Coordination Chemistry Reviews 439 (2021) 213924

Contents lists available at ScienceDirect

Coordination Chemistry Reviews

journal homepage: www.elsevier.com/locate/ccr

Review

Ultrafine metal species confined in metal–organic frameworks: Fabrication, characterization and photocatalytic applications

Jiao Cao [a,b], Zhaohui Yang [a,b,*], Weiping Xiong [a,b,*], Yaoyu Zhou [c], You Wu [a,b], Meiying Jia [a,b], Chengyun Zhou [a,b], Zhengyong Xu [d]

[a] College of Environmental Science and Engineering, Hunan University, Changsha 410082, PR China
[b] Key Laboratory of Environmental Biology and Pollution Control (Hunan University), Ministry of Education, Changsha 410082, PR China
[c] College of Resources and Environment, Hunan Agricultural University, Changsha 410128, PR China
[d] Hunan Provincial Science and Technology Affairs Center, Changsha 410013, PR China

ARTICLE INFO

Article history:
Received 15 October 2020
Accepted 14 March 2021

Keywords:
Metal-organic frameworks
Metal species
Characterization
Photocatalysis
Synergistic effects

ABSTRACT

Photocatalysis, which can be utilized for H_2 production, CO_2 reduction, and water remediation, promising a bright future in addressing energy and environmental challenges. Metal-organic frameworks (MOFs) with highly uniform crystal structures provide internal conditions to restrain the aggregation of metal species and generate the composite with superb stability. Such confinement strategy offers advantages in designing of photocatalysts with abundant active sites, increased mass-transfer efficiency, enhanced light adsorption and high photo-generated carriers utilization rate due to the synergistic effects. Here, the recent advances in fabricating metal species confined in pores of MOFs are concluded. Advanced characterizations for characterizing the relative location between metal species and MOFs are displayed. Moreover, the photocatalytic applications of metal species@MOFs in energy and environment and the corresponding photocatalytic mechanisms are discussed. Challenges and perspectives are given, with good hope to promote the development of fabricating advanced and efficient photocatalyst.

Contents

* Corresponding authors at: College of Environmental Science and Engineering, Hunan University, Changsha, Hunan 410082, PR China.
E-mail addresses: yzh@hnu.edu.cn (Z. Yang), xiongweiping@hnu.edu.cn (W. Xiong).

https://doi.org/10.1016/j.ccr.2021.213924
0010-8545/

1. Introduction

Currently, environmental contamination and energy shortage have caused severe problems in human production and life. The total energy consumption in the 2010s was counted as 524 quadrillion British thermal units (Btu) which were mainly derived from fossil fuels [1], resulting in excessive carbon dioxide (CO_2) emission (about 30 Gt per year) [2]. However, as expected, the value can grow to 630 quadrillions Btu and even 820 quadrillions Btu in the 2020s and 2040s, respectively [3,4]. The data from the International Energy Agency revealed the mean atmospheric CO_2 concentration was 400 ppm in 2018, while the value may increase to 950 ppm around 2100 [5]. On the other hand, with the rapid growth of textile and apparel industries, a large number of dyes are widely utilized. According to statistics, there are around 7×10^5 tonnes (exceed 10,000 types) of consumption per annum [6]. The effluent of dye wastewater in the water-cycling system is of concern for their high chroma, toxicity, which makes it hard to be biodegraded. Metal species photocatalysis is considered to be a potential strategy for hydrogen (H_2) generation, carbon dioxide (CO_2) reduction and contamination degradation, which will play a crucial part in environment purification and energy conversion. Despite the achievement, metal leaching, low stability and uncontrolled activity of metal species photocatalyst still need to be resolved.

Inspired by the spheroproteins in enzyme, larger enzyme encapsulates the active spheroproteins usually offer a confined environment, the active sites and local microenvironments exert incredible control over catalytic reactions [7,8]. Moreover, the confined enzymes can utilize the cavity and the contained groups to adjust the substrates selectivity and catalytic activities [9]. The confinement strategy refers to the active species encapsulated in the porous support and the porous support limits the active species into nanometer size, which is proved to be efficient for stabilizing active sites and improving photocatalytic activity for quantum size effect and synergistic effect [10–13]. In recent years, confined strategies based on carbon nanotube (CNT) have important advantages in catalytic reactions due to their unique structure of nanocavities formed by the curved graphene walls [14]. Pan et al. [15] compared the Fenton-like process catalyzed by Fe_2O_3 nanoparticles confined in multiwalled carbon nanotubes (Fe_2O_3@-FCNT-H) and Fe_2O_3 nanoparticles loaded on the outer surface (Fe_2O_3/FCNT-H). Results showed the confined strategy greatly enhanced the catalytic property and the confinement changed the reaction pathway both kinetically and thermodynamically. However, the sizes and morphologies of inner metal species, the properties of supports, and the interactions between the inner active species and outer supports were closely related to the performance [16]. The ideal environment surrounding metal catalysts should be both structurally and chemically stable and flexible, enabling the efficient transfer of reactants to the active sites [8]. Therefore, the controllable preparation of metal species with uniform distribution and ultrasmall size under confinement is an important basis for investigating the structure–function relationship of photocatalysts and improving the photocatalytic activity.

Metal-organic frameworks (MOFs) consisted of metal centers/-clusters and organic ligands, the periodic and well-organized pore structure, uniformly distributed active sites and relatively high stability make them with promising applications in the photocatalytic process [17–19]. MOFs have been considered as efficient supports to confine small metal species, like metal nanoparticles (NPs), metal oxides, quantum dots (QDs), polyoxometalates (POMs) and metal phosphides [20,21]. The highly ordered porous structures and adjustable crystal morphologies offered internal conditions to restrain the aggregation of metal species and generate MOFs-confined uniform metal species with superb stability, and the diverse functional groups were beneficial for various interactions with reacting molecules [22–24]. Moreover, the diversified metal/organic compositions make it possible to fabricate MOFs with tunable pore structure and electronic properties, which make for the investigation of photocatalytic mechanism [25,26]. Thus, MOFs provided a novel strategy for fabricating composite photocatalysts under confinement with improved or new properties compared to the pristine MOFs, which has inspired the study of new functional materials.

This review has summarized the recent progress of metal species@MOFs. First, the controllable synthetic method of metal species confined in the pores of MOFs are presented. Second, advanced characterization techniques for investigating the relative location between metal species and MOFs are described. Third, interactions between inner metal species and outer MOFs are discussed when introduces photocatalytic applications in the environment and energy fields. Challenges and outlooks are discussed at the end of the article, in short, MOFs confined strategy are promising in the field of photocatalysis.

2. Synthetic strategies for metal species confined in MOFs

The highly tunable structure and composition of MOFs make it possible for controllable synthesis of metal species evenly confined in the pores of MOFs. The novel strategy of controllable location, composition, and size of metal species confined within MOFs should be developed. Generally, the synthetic strategy can be divided into prefabrication of MOFs, pro-fabrication of MOFs and one-pot fabrication. Besides, due to the regular arrangement of metal sites, MOFs can act as a self-sacrifice template to in-situ transform the partial metal sites into metal species and confined in the MOFs while the structure of the pristine MOFs is retained. The traditional methods still exist some disadvantages like low loading efficiency and high agglomeration of metal species, some novel design should be developed. In the following sections, the novel design principles and synthetic strategies of metal species confined MOFs composites in terms of structure and composition are discussed.

2.1. Prefabrication of MOFs

The highly ordered structure and the definite nanopores of MOFs offer metal species a microenvironment for confining them through a "ship in bottle" strategy [27], which means the prefabrication of MOFs and then encapsulate the metal precursor in the channels or cavities of MOFs. Therefore, an appropriate amount of metal precursor is needed to ensure their complete introduction into the pores or channels of MOFs. In addition, the subsequent reduction process must be conducted quickly to prevent agglomeration. The traditional synthetic methods like impregnation method, vapor deposition and solid grinding will inevitably result in the massive loading of metal species on the external surface of MOFs due to the microstructure of MOFs and the interaction between MOFs and the metal species. On the other hand, the content of metal precursors and experiment conditions will affect the location of metal species. Therefore, other assisted methods like ultrasound, microwave, supercritical CO_2-assisted method [28] should be applied and some novel methods need to be utilized. Moreover, the stability of the host MOFs should be considered.

2.1.1. The impregnation method

The impregnation method involves MOFs host immersing in the solution containing metal precursor. With the capillary pressure,

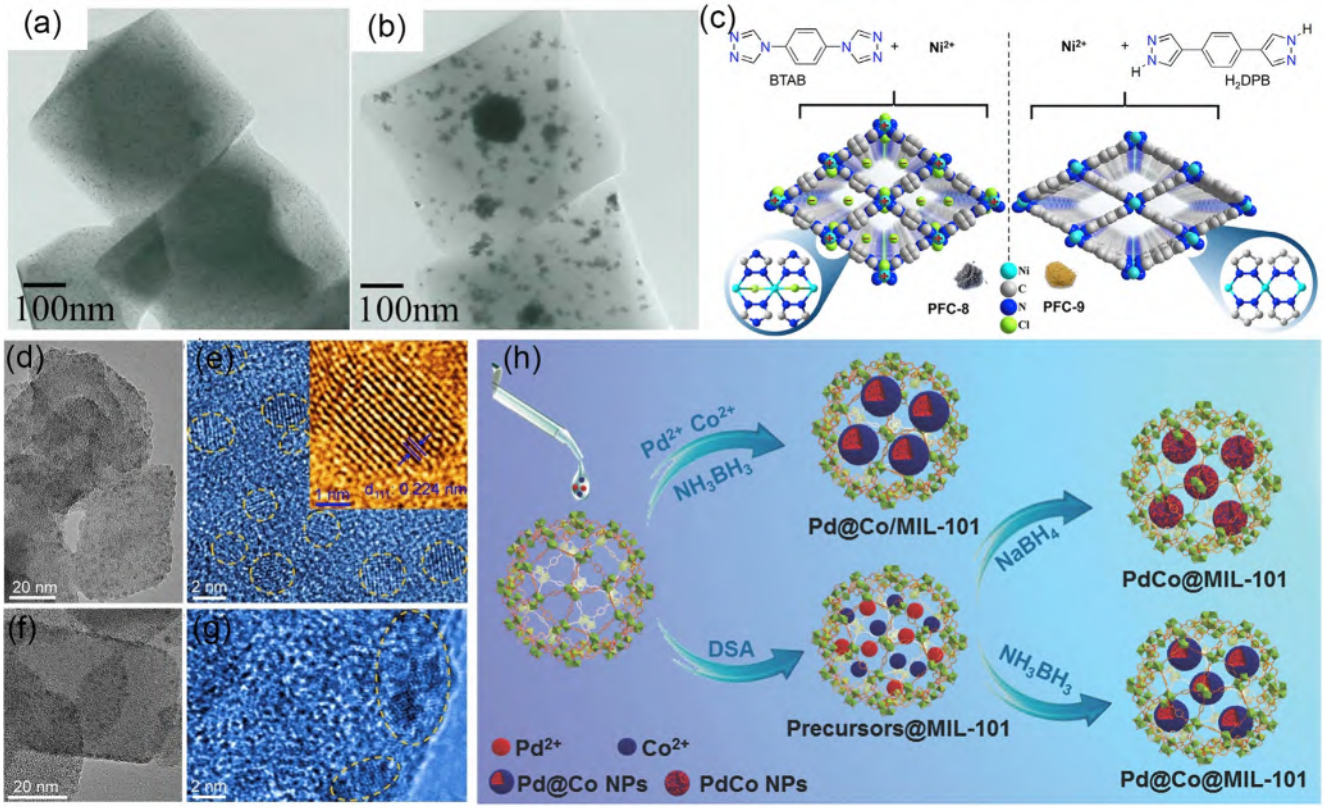

Fig. 1. TEM images of Pt@MIL-101(Cr) prepared by $scCO_2$-assisted immobilization (a) and Pt@MIL-101(Cr) prepared by conventional immobilization (b). Reproduced with permission [35]. Copyright 2016, Elsevier. Structures of cationic PFC-8 and neutral PFC-9 (c); Bader charge analyses for the Ni^{II} center and the coordinated nitrogen and chlorine atoms in PFC-8 and PFC-9 (d); Computational optimized configurations and binding energies of a proton with the ligands in PFC-8 (e-h) and PFC-9 (i); HRTEM images of Pd@PFC-8 (j and k); HRTEM images of Pd@PFC-9 (l and m). Reproduced with permission [40]. Copyright 2020, Wiley; the synthetic process of Pb@Co@MIL-101 (h). Reproduced with permission [46]. Copyright 2015, Wiley.

the metal precursor infiltrates into the inner surface of MOFs. Though the impregnation method can be performed in a mild condition, the good match of metal precursor diameter and pore size of MOFs is required to be considered [29]. In addition, the competition between the metal precursor and solvent molecules can result in the uneven particle size distribution [30]. By enlarging the pore size of MOFs can facilitate the confinement of metal precursors. Zhang et al. [31] found that some of the functionals groups in UiO-66 can be removed by pyrolytic treatment and the pore size was enlarged at the same time. Therefore, the neutral iron acetylacetonate can be confined in UiO-66 and then generated α-Fe_2O_3 nanoclusters (2 nm). They also found that the selection of metal precursor was essential as the positive $FeCl_3$ was hard to be absorbed in pores of UiO-66. Moreover, the defect-engineering strategy can be applied for binding metal precursors on the defective sites of MOFs. Yaghi et al. [32] fabricated the monatomic Cu confined in UiO-66. The defective UiO-66 can covalently interact with Cu atoms on the defect sites of Zr-O sites.

Some assisted methods can be utilized to adjust the diameter and location of metal species. Aslam et al. [33] fabricated Ni NPs (<2 nm) of 20 wt% content to be confined in micromesoporous MIL-101(Cr) with high dispersion via an ultrasonic assisted impregnation method. MIL-101 possessed large aperture (1.1–2.5 nm) and high pore volume (1.9 $cm^3\ g^{-1}$), which was beneficial for permeating Ni precursor and the ultrasonic aid was contributed to the high dispersion of Ni precursor. Due to the high diffusivity and low viscosity of supercritical CO_2 ($scCO_2$), the $scCO_2$ assisted impregnation method makes for uniformly decoration and impregnation of metal precursors into the pores of MOFs [34]. Matsuyama et al. [35] developed a supercritical CO_2 ($scCO_2$) assisted impregnation method to confine ultrafine Pt NPs (2–3 nm) in the pores of MIL-101(Cr) and no Pt NPs aggregated (Fig. 1a). Because of the $scCO_2$ assisted impregnation method, the inner surface of MIL-101(Cr) enhanced a little. When utilized the traditional impregnation method, the mean diameter of Pt NPs in Pt@MIL-101(Cr) was 10.7 nm and most of Pb NPs agglomerated on the external surface of MIL-101(Cr) (Fig. 1b). Due to the complicated pore structure of MIF-101(Cr), it was hard for impregnating enough Pt precursor into the pores.

Most of the MOFs are electrically neutral as the positive-charged metal ions are neutralized by the negative-charged organic linkers [36]. However, there are some cases of ionic MOFs (iMOFs) of which the frameworks are cationic or anionic with counterions in the channels [37]. IMOFs result from the mis-charged net charge of the skeleton, which needs extra charged species to keep the overall electrically neutrality. Such iMOFs are attaining considerable attention as the charged species in the skeleton can be applied for the attractive electrostatic interactions with various encapsulated guest ions in the channels and improved host–guest interactions. Electrostatic interaction between the different surface charge of MOFs and metal precursors can effectively drive the self-assembly of materials [38,39]. Huang et al. [40] fabricated cationic PFC-8 and neutral PFC-9 (PFC = Porous materials from FJIRSM CAS) with similar dative bonds, space groups, and topologies (the structures were shown in Fig. 1c). Excepted for the higher chemical stability, the counterions in PFC-8 can be replaced by $PdCl_4^{2-}$ followed with $NaBH_4$ reduction to fabricate ultrafine Pd nanoparticles evenly confined in PFC-8 composite (Pd@Nano-PFC-8) with a mean diameter of 1.75 nm (Fig. 1d and e). However, most of Pd NPs were found in the edge of PFC-9

(Fig. 1f and g). Therefore, the electrostatic interaction between cationic PFC-8 and $PdCl_4^{2-}$ was contributed to the ion-exchange process and even confinement of $PdCl_4^{2-}$ precursor. Moreover, the porous cationic charged framework of PFC-8 can withstand the harsh reductive condition in $NaBH_4$ and provided a confinement effect preventing nanoparticles from aggregation. In this regard, the electrostatic attraction method is the use of desired metal ions confined in opposite charged MOFs with suitable neutral bridging ligands.

The double solvents method (DSM) is carried out by using plentiful of hydrophobic solvent combined with hydrophilic solvent to force metal precursors confined in the pores of MOFs [41]. To ensure the complete confinement of metal precursors in the pores of MOFs, the amount of metal precursor solution must be less than the pore volume of MOFs. The selected MOFs should be stable and have large cavity size and pore volume for better introduction of metal precursor and then reduced them into pores. The combination of DSM and overwhelming reduction can confine metal species in the pores of the MOFs and greatly minimize metal species aggregation on the outer surface [42] The controlling of size and location of metal species can be achieved by controlling the amount of metal precursors and reductants [43]. Xu et al. exploited a liquid-phase concentration-controlled reduction strategy to adjust the size and location of the AuNi NPs [44]. As the internal surface area of MIL-101(Cr) was higher than the external surface area, a small number of Au^{3+} and Ni^{2+} precursors solution suspended in a mass of anhydrous n-hexane was introduced to the hydrophilic pore by capillary force. Then, the overwhelming reduction approach with $NaBH_4$ can make the ultrafine AuNi alloy NPs (1.8 ± 0.2 nm) be confined in the MOFs nanopores. In contrast, serious agglomeration of metal species occurred with a moderate method of low $NaBH_4$ concentration. Consequently, the key was the amount of metal precursors and $NaBH_4$ concentration. The volume of metal precursors was little than the pore volume of adsorbent and $NaBH_4$ concentration should be high to prevent metal species to be aggregated on MIL-101(Cr) surface [45]. Interestingly, Jiang et al. [46] found that selecting the appropriate reducing agent combined with double solvents approach (DSA) can confine core–shell metal species into MOFs. As showed in Fig. 1h, after pre-incorporated Pd^{2+} and Co^{2+} precursors into MIL-101(Cr) pores via DSA, the selection of reducing agents of the following reduction process affected the final product. When used NH_3BH_3 as reducing agent, the Pd NPs cores were formed at first, then the Co NPs shells were formed and encapsulated the Pd NPs to generate Pb@Co NPs (~2.5 nm). The different reduction potentials of Pb^{2+} ($E^{02+}_{Pb/Pb}$ = +0.915-eV vs SHE (Standard Hydrogen Electrode)) and Co_{2+} ($E^{02+}_{Co/Co}$ = −0.28 eV vs. SHE) made the NH_3BH_3 reduced Pb NPs at first and then reduced Co^{2+} by M−H species generated from NH_3BH_3 hydrolysis and finally synthesized Pb@Co@MIL-101(Cr). However, when used $NaBH_4$, a stronger reducing agent, the pre-incorporated Pd^{2+} and Co^{2+} were transformed to PdCo alloy NPs (~2.5 nm) in the pores of MIL-101 (Cr) (PdCo@MIL-101(Cr)). On the contrary, when the Pd^{2+} and Co^{2+} precursors were reduced by NH_3BH_3 directly, the Pd@Co NPs (3.0–3.5 nm) would be loaded on the outer surface. Therefore, the combination of the double-solvent method and overwhelming reduction was facile and effective to adjust the confinement of the metal species with ultrafine size into MOFs matrices possessing hydrophilic pores.

In general, the metal precursors in MOFs undergo the reduction process by $NaBH_4$ or H_2 to form metal species. The redox-active MOFs can in-situ reduce the metal precursors and confine them in MOFs. The in-situ reduction process can avoid the inhomogeneity of reducing reagents, which was made for the generation of highly-dispersed, ultra-small metal species [47]. Zhou et al. [48] synthesized two redox-active MOFs, which named compounds 1 ($[Zr_6(TTFTB)_2O_8(OH_2)_8]$) and 2 ($[Zr_6(Me\text{-}TTFTB)_{1.5}O_4(OH)_4(C_6H_5COO)_6]$) (TTFTB = tetrathiafulvalene tetrabenzoate; Me-TTFTB = tetrathiafulvalene tetramethylbenzoate).

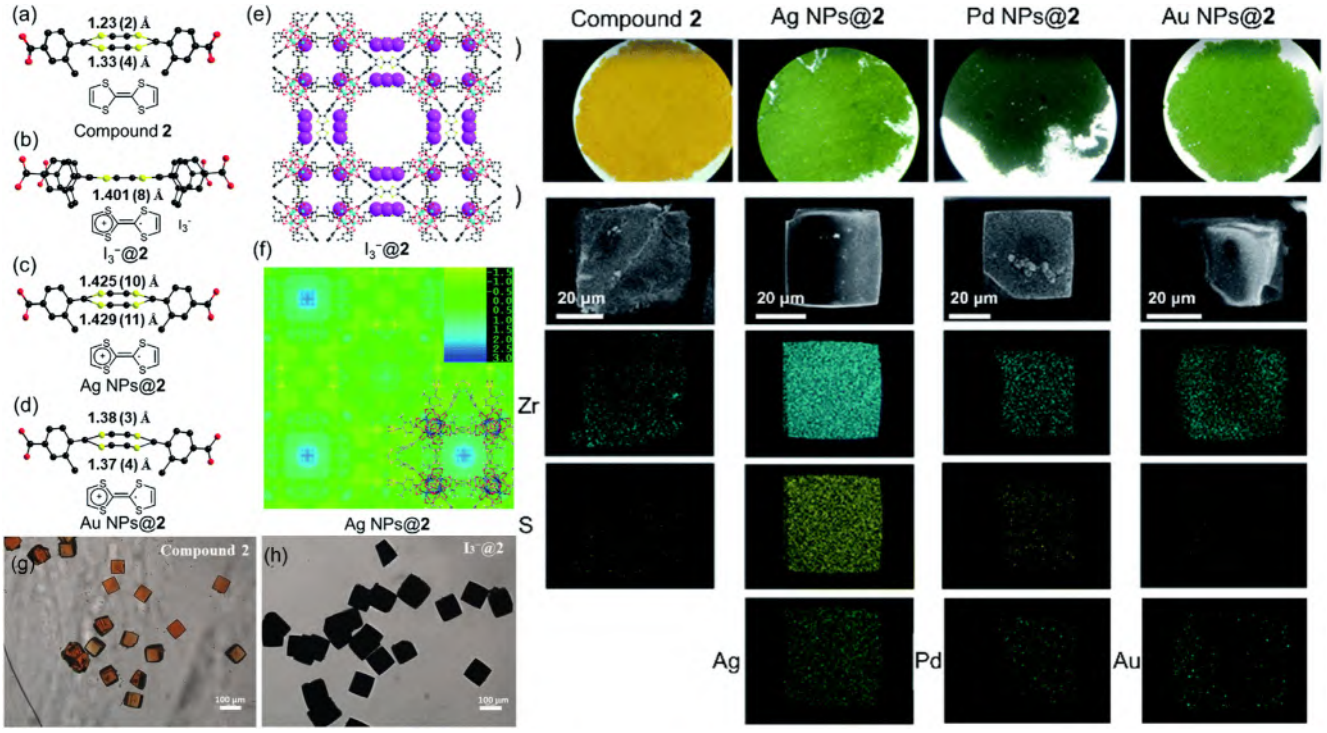

Fig. 2. The conformation of Me-TTFTB in the single crystal structure of 2 (a), I_3^-@2 (b), Ag NPs@2 (c) and Au NPs@2 (d); (e) I_3^- locations in the single crystal structure I_3^-@2; Photographs of compound 2 before (f) and after (g) was soaked in a cyclohexane solution of I_2; (h) Optical microscope images, and element mapping of Ag NPs@2, Pd NPs@2, and Au NPs@2 under SEM/EDX (i). Reproduced with permission [48]. Copyright 2020, Royal Society of Chemistry.

The TTF-moieties with highly electron-donating nature showed lower redox potential than most noble metal ions like Ag^{+}, Au^{3+}, Pt^{2+}, Pd^{2+}, Ru^{3+}, Ir^{3+}. Owing to the reductive TTF-moieties, the Ag^{+}, Pd^{2+}, and Au^{3+} ions in solution can be in-situ reduced to ultra-small Ag, Pd, and Au NPs, respectively and confined in the cavities of compounds 1 and 2. As the TTF-moieties were evenly distributed in MOFs, the aggregation of metal species can be minimized. Moreover, the sulfur-rich pore environment of MOFs acted as a support to stabilize and confine the generated metal species. Take compound 2 as an example, after treated by I_2 (Fig. 2f and g), a visual color change from orange to black can be found, which may because of the presence of $TTF^{\cdot+}$ and I_3^- species, the I_3^- species were the oxidation product (Fig. 2e). Compared to the pristine compound 2, the centric C–C distance increased to 1.401 (8) Å (Fig. 2a and b) as the double bonds in neutral TTF transferred to single bonds in $TTF^{\cdot+}$. A similar change can be observed in Ag NPs@2 and Au NPs@2 (Fig. 2c and d). In addition, after loading metal species, the color of powder changed from yellow to green (Fig. 2h) and the optical images of samples presented the metal species was highly distributed in compound 2 (Fig. 2i). Nobel metal species (such as Ag, Au and Pt) can be generated by photo-deposition that NPs can in-situ generate in MOFs by applying the light beam to realize the reduction process [49]. In addition, microwaving irradiation also can be applied to reduce the metal precursors into metal species [50].

2.1.2. Vapor deposition

Vapor deposition is carried out by infiltrating volatile metal precursor into the pores of MOFs host which is solvent-free. The vapor deposition strategy showed a potentially faster metal loading. However, this method depends on the vapor pressure and operation temperature, the structure of MOFs host may be partially broken. The MOFs host should be stable in high pressure and temperature. Moreover, vapor deposition allows plentiful loading of metal species, while it is difficult to adjust the size and location without aggregation [51]. Therefore, the vapor deposition method is relatively complicated to operate and the volatile metal precursor is usually expensive.

Xu et al. [52] found that compared to liquid deposition, the vapor deposition method was better to prepare highly-dispersed Ni NPs confined in ZIF-8. They fabricated Ni@ZIF-8 through sequential deposition-reduction methods (the synthetic process was performed in Fig. 3a), named as 1-Ni@ZIF-8 (fabricated via vapor deposition) and 2-Ni@ZIF-8 (fabricated via liquid deposition). 1-Ni@ZIF-8 was fabricated by putting ZIF-8 and $Ni(cp)_2$ (a small volatile molecule nickelocene) in separate small glass vessels and placed together in a Schlenk tube to be vacuum heated, followed by H_2 treatment. 2-Ni@ZIF-8 was fabricated via mixing the methanol suspension of ZIF-8 and diethylether solution of Ni $(cp)_2$ and removing the solvents by natural evaporation, then reduced by H_2. Interestingly, from the TEM and HAADF-STEM images, the Ni NPs were uniformly distributed in 1-Ni@ZIF-8 and 2-Ni@ZIF-8, while the average diameters were 2.7 ± 0.7 and 4.5 ± 1.0 nm, respectively. A slight aggregation existed in 2-Ni@ZIF-8. In addition, the cavity-conform Pd NPs can be confined in MIL-101 by vapor deposition applying the $[(C_5H_5)Pd(C_3H_5)]$ precursor followed by H_2 reduction at room temperature (Fig. 3b, left), while significantly smaller Pd NPs were formed at the reduction temperature of 70 °C (Fig. 3b, center) [53]. Therefore, the remaining space was existed to confine another metal to obtain bimetallic NPs and the Pd NPs can serve as agglomeration sites (Fig. 3b, right). However, the simultaneous confinement of bimetallic NPs was difficult for the various reduction behavior of metal precursors. The fabrication of Pd_xNi_y@MIL-101 composites was generated by substituting

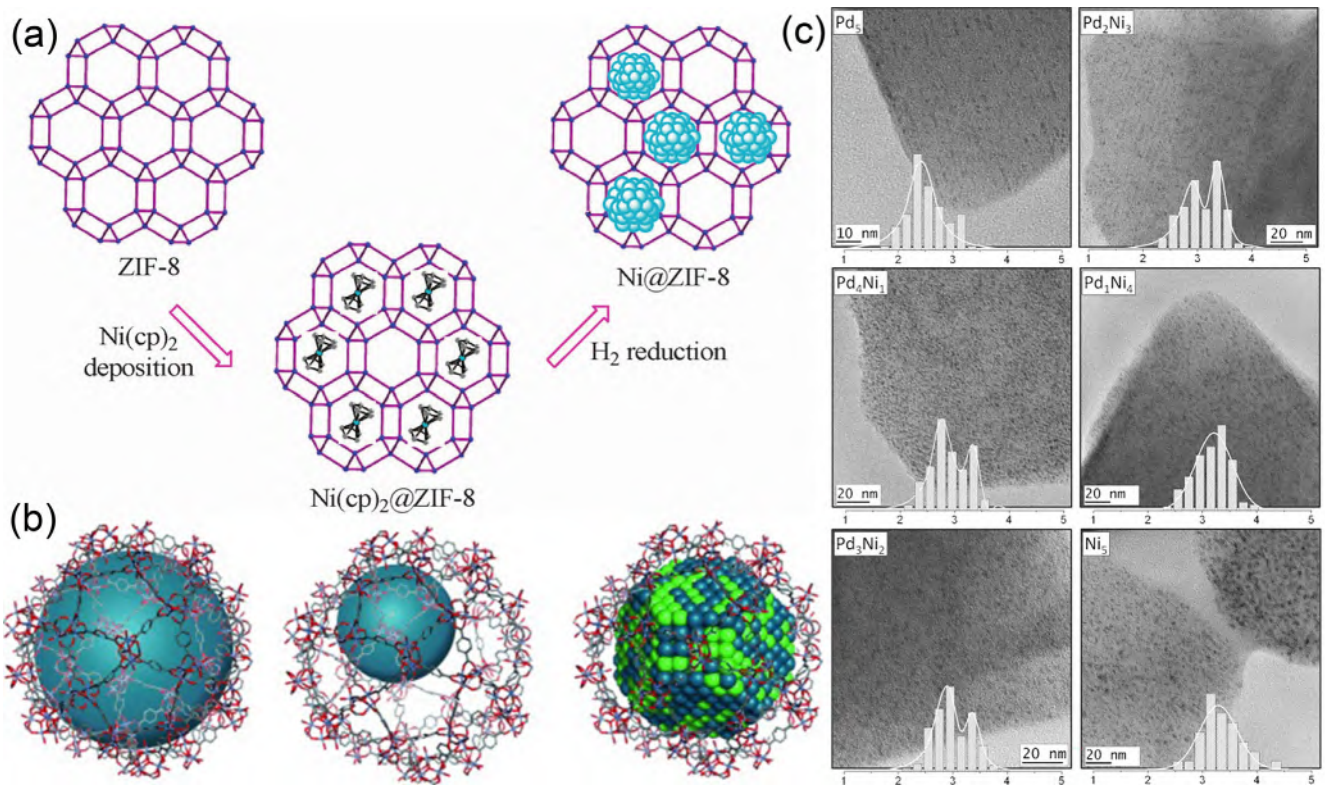

Fig. 3. (a) Schematic illustration of preparation of Ni@ZIF-8. Reproduced with permission [52]. Copyright 2012, Royal Society of Chmistry; (b) Size-selective cavity loading of MIL-101 (left: cavity-conform; center: undersized cavity loading; right: introduction of a second metal); (c) TEM investigations of the Pd_xNi_y@MIL-101 catalyst systems using the optimized reduction conditions (the reduction time was 20 h; Pd_5, Pd_4Ni_1, Pd_3Ni_2 = 70 °C/50 bar; Pd_2Ni_3 = 70 °C/5 bar; Pd_1Ni_4, Ni_5 = 90 °C/5 bar). Reproduced with permission [53]. Copyright 2012, Wiley.

Pd by Ni in 20 wt% and optimizing the reduction condition. The TEM images (Fig. 3c) showed the particle sizes of different NPs were around 3 nm and the NPs were highly dispersed in the layer of MIL-101.

The Zr_6-based NU-1000 with large pores alongside accessible –OH and $–OH_2$ groups on the Zr_6 node attributed to the targeted dispersion of metal precursor. The excellent thermal and hydrolytic stability made the NU-1000 suitable for vapor deposition strategy [54]. Hupp et al. [55] fabricated Cu NPs@NU-1000 with a good match of the pore width of NU-1000 and Cu NPs. During the vapor deposition process, the $Cu(dmap)_2$ precursor (dmap was dimethylamino-2-propoxide) permeated the NU-1000 and reacted with –OH and $–OH_2$ groups on the Zr_6 nodes. After treated in H_2 atmosphere, the Cu(II) reduced to Cu(0), the Cu(0) lacked Zr(IV)-O(H)-Cu(II) linkage and then agglomerated to generate NPs. The Cu NPs eventually stopped agglomerating as the limitation of the widths of the NU-1000 channels. The average diameter of Cu NPs was around 3.2 nm, basically the same as the size of hexagonal channels in NU-1000 (3.1 nm). Martinson et al. chosen 16 metal precursors such as metal alkyls, alkylamides and metallocenes to study the loading of metal species in the pores of NU-1000 [56]. The confined metal species should be spatially uniform and the NU-1000 framework should be structurally complete. Therefore, the selection of metal precursors and MOFs was important. Moreover, they found that partial pressure and exposure time had an effect on the special distribution of metal precursors.

2.1.3. Solid grinding

Solid grinding has been identified as a facile way to introduce metal precursor into the pores of MOFs without waste solvent, the solid-state compounds are mixed completely [57]. During the grinding process, the metal precursors rapidly diffuse into the pores or channel of MOFs. After further treating, the metal species@MOFs can be obtained [30]. Typical solid grinding is to grind solid-state compounds, either manually in an agate mortar or utilizing electric machinery (such as ball mills or other grinding machines). Many researchers are interested in the solid grinding of MOFs for easy operation, high yield and flexible feeding, which is expected to be massively produced. In addition, solid grinding can effectively solve the problem of poor solubility of reactants and solid reactants with low solubility such as sulfate, carbonate and even oxides and hydroxides can be used as precursors [58]. In spite of the easy operation of the solid grinding method, the solid-phase reaction lacked control in the growth of metal species and the volatile metal precursors are generally expensive.

Haruta et al. [59] found that the solid grinding was effective for confining Au NPs in MOFs, including MOF-5, CPL-1 ($[Cu_2(pzdc)_2(pyz)]n$, pzdc = pyrazine-2,3-dicarboxylate, pyz = pyrazine), CPL-2 ($[Cu_2(pzdc)_2(bpy)]n$, bpy = 4,4′-bipyridine), Al-MIL-53 ([Al(OH)(bdc)]n), and Cu-BTC ($[Cu_3(btc)_2]n$ (btc = benzene-1,3,5-tricarboxylate). A certain amount of volatile Dimethyl acetylacetonato gold (III) complex ($Me_2Au(acac)$) and MOFs were ground in air at room temperature. Subsequently, the compound was reduced by H_2 to obtain Au/MOFs. The Au/CPL-2 synthesized by solid grinding method possessed small Au NPs (2.2 nm ± 0.3 nm) with uniform distribution while the larger Au NPs (3.1 nm ± 1.9 nm) existed in Au/CPL-2 synthesized by vapor deposition. Compared to the vapor deposition method that took a long time (about 6 h) to vaporize the Au precursor, the solid grinding method made the $Me_2Au(acac)$ sublimate rapidly and uniformly distribute into MOFs support. Notably, in the vapor deposition process, the diffusion of Au precursor was heterogeneous as the MOFs support was unstirred, which leaded to the formation of larger Au NPs. Moreover, different kinds of MOFs support were related to the size of Au NPs and the Au NPs in Au/Al-MIL-53 showed the smallest size (the average size was 1.5 nm ± 0.7 nm).

Diaz et al. [60] incorporated Ag NPs into mesoporous MIL-100 (Fe) through solid grinding, incipient wetness and ion exchange liquid impregnation. They found that the solid grinding method leaded to the generation of Ag NPs with larger size and heterogeneous distribution on the outer surface of the MIL-100(Fe), few Ag NPs embedded in MIL-100(Fe). However, the wetness impregnation and ion exchange methods embedded abundant Ag NPs in MIL-100(Fe) pores and presented a more homogeneous distribution of Ag NPs. Therefore, some specific MOFs can be used for better confinement of metal species through solid grinding method. Maji et al. [61] applied anionic perovskite MOFs [MA-M$(HCOO)_3$] (MA = methylammonium cation, M = Mn and Co) for the confinement of lead halide ($MAPbBr_3$) perovskite quantum dots (PQDs) via Pb^{II} encapsulation (the synthetic process was showed in Fig. 4a and the structure of MA-M$(HCOO)_3$ was performed in Fig. 4b). The XRD analysis showed the existence of $MAPbBr_3$ and MOFs in the composite (Fig. 4c). The peaks at 2θ = 15, 30.1, 33.7, and 43.08° in the XRD belonged to the (110), (200), (210), and (220) crystal faces of $MAPbBr_3$. Moreover, from the TEM images, the $MAPbBr_3$ PQDs were uniformly dispersed in MOFs and the particle size in MA-Mn$(HCOO)_3$ and MA-Co$(HCOO)_3$ were 5–8 nm and 8–10 nm, respectively (Fig. 4d and f). HRTEM images showed the PQD with a lattice spacing of 0.29 nm, which corresponding to the (110) crystal face in $MAPbBr_3$ (Fig. 4e and g). During the grinding process of MOFs and $PbBr_2$, the weak noncovalent interactions between MOFs and MA can be replaced by the stronger interaction between MA and $PbBr_2$. The anionic perovskite MOFs not only served as a support to confine the NPs, but also provided MA source for the formation of the $MAPbBr_3$ QDs.

2.2. Post-fabrication of MOFs

The biggest problem of the prefabrication of MOFs method is to overcome the diffusion resistance between the inner and outer surface of MOFs to ensure the uniform distribution of metal precursors in MOFs pores. The post-fabrication of MOFs strategy is fabricating MOFs around the metal species or its precursor. Compared with the prefabrication of MOFs method for fabricating of metal species confined composites, fabrication of metal species prior to MOFs can better control the size, morphology, composition of metal species. Despite the advantages, the fabrication of uniformly distributed and controllable metal species-confined composites via post-synthesis of MOFs is a significant challenge [30].

The hot-pressing method was carried out under appropriate temperature and pressure that the MOFs precursors can be rapidly transferred to a highly stable crystal [62]. Wang et al. [63] applied a solvent-free in-situ hot-pressing method to confine $H_3PW_{12}O_{40}$ (PW_{12}) in the pores of MFM-300 (In) by physical imprisonment (Fig. 5a). Typically, $In(NO_3)_3{\cdot}5H_2O$, H_4BPTC (biphenyl-3,3′,5,5′-tetra-carboxylic acid) and PW_{12} were grinded for 5 min, then the powders were covered by aluminum foil and packed with an electric iron at 80 °C for 10 min. The rapid nucleation of MFM-300 (In) around PW_{12} was time/energy-saving and the method can be applied in massive production.

In general, the introduction of a bridge layer of linker and/or surfactant molecules between MOFs and metal species facilitates the generation of confinement-structured metal species@MOFs as the reduced aggregation via supplement of additional charge and/or steric repulsion [64]. The surface functionalization of metal species before encapsulated them into the MOFs can improve the interactions between MOFs and metal species and facilitate the dispersion of metal species during the formation of MOFs [65]. Lu et al. proposed a controlled encapsulation method for fabricating metal species (such as Au, Pt, CdTe, Fe_3O_4, La-doped $NaYF_4$, Ag cubes, β-FeOOH rods) of various size confined in ZIF-8 with high dispersion [66]. The metal species were coated with

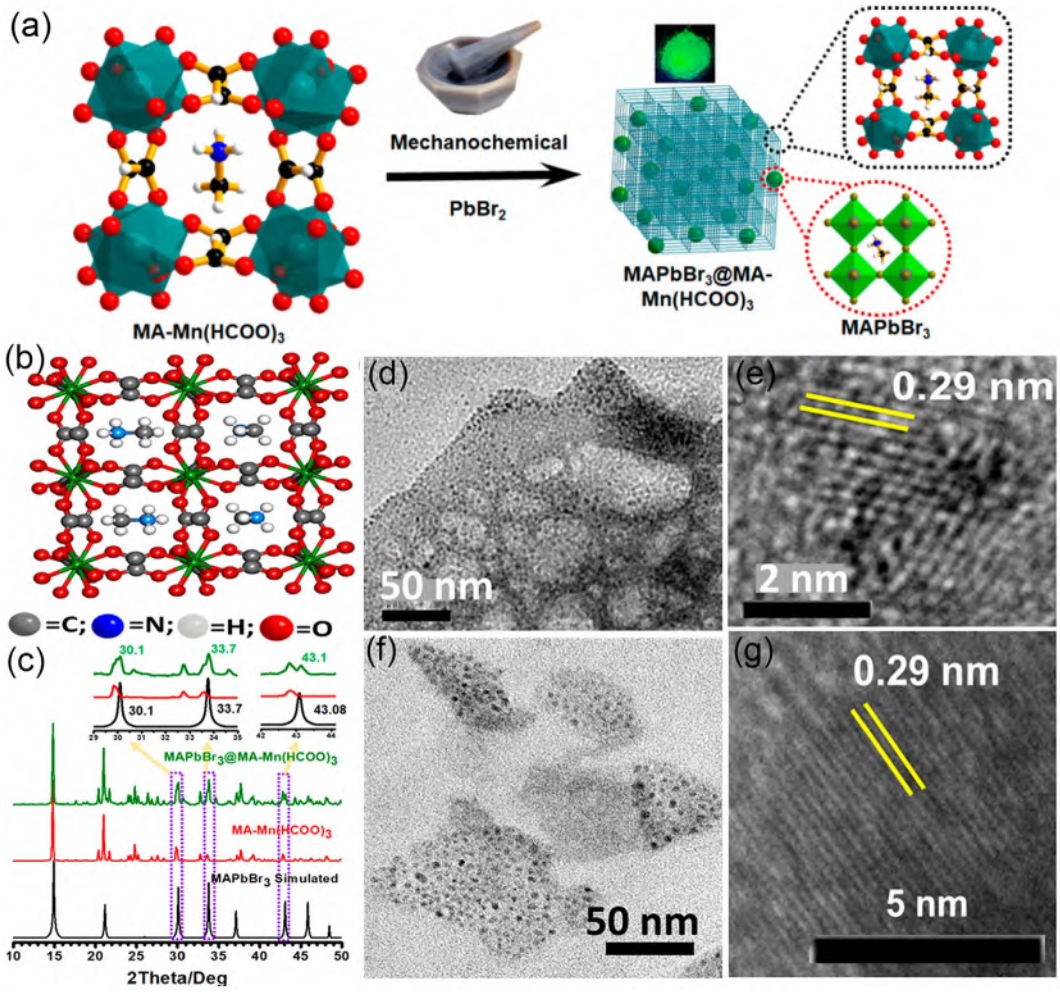

Fig. 4. (a) Strategy for synthesis of $MAPbBr_3$ QDs on a perovskite MOF ($MAPbBr_3$@MA-Mn$(HCOO)_3$); (b) 3D structure of MA-M$(HCOO)_3$; (c) Comparison of PXRD patterns of MA-Mn$(HCOO)_3$ and $MAPbBr_3$@MA-Mn$(HCOO)_3$; (d) TEM and (e) HRTEM images of $MAPbBr_3$@MA-Mn$(HCOO)_3$; (f) TEM and (g) HRTEM images of $MAPbBr_3$@MA-Co$(HCOO)_3$. Reproduced with permission [61]. Copyright 2020, American Chemical Society.

polyvinylpyrrolidone (PVP) and then ZIF-8 was crystallized around them. PVP was an amphiphilic polymer, the PVP-coated metal species was more stable in polar solvents and showed improved affinity to MOFs [67]. The PVP favored the continually generating fresh surfaces of the growing MOFs and the metal species can attach to the growing MOFs without changing their structure. Other capping agents like cetyltrimethylammonium bromide (CTAB) [68] had been proved to be effective as it can act as a "soft template" to generate mesopores in MOFs, as well as built uniform voids throughout MOFs framework to control the particle size and stabilize metal species. Notably, the time of metal species introducing was critical. Changing the dosage of metal species initially introduced to the reaction and the synthetic condition of MOFs to ensure metal species were entirely confined in the MOFs and adjusted the final content of metal species. Despite the advantages, the capping agents were difficult to be completely removed, which may result in more ambiguous interfaces between MOFs and metal species and formed a physical barrier that prevented the reactants from accessing to active sites.

Metal precursor-supported metal species composites can be in-situ sacrificed to generate metal species@MOFs, the metal species were confined in MOFs during the sacrificial process, which avoided the homogeneous growth of MOFs and the use of stabilizing agents. Li et al. [69] fabricated Pd@ZIF-8 by using ZnO (~20 nm) as the metal precursor. Firstly, the ZnO was mixed with $PdCl_2$ and $PdCl_2$ was dispersed on the ZnO surface in solid state. After H_2 treatment, Pd NPs were generated on ZnO surface (Pd/ZnO). Then, the Pd/ZnO were reacted with 2-methylimidazole (H-mim) by ball milling and sacrificed to generate Pd@ZIF-8 (Fig. 5b). The XRD patterns showed the characteristic peaks of Pd@ZIF-8 were fitted with the ZIF-8 and hardly any peaks belonged to ZnO were observed (Fig. 5c). Therefore, most of ZnO was transferred to ZIF-8 and the obtained Pd@ZIF-8 inherited the crystal texture of ZIF-8. Compared to Pd/ZnO, the characteristic peak belonged to Pd at 40.1° in Pd@ZIF-8 was disappeared may because of the confinement of Pd in ZIF-8. N_2 adsorption–desorption isotherm showed the Pd@ZIF-8 exhibited a similar pore structure to ZIF-8 of type I curve and the BET surface area of samples was close (Fig. 5d). Thus, the Pd confinement did not cause the damage to ZIF-8 crystal, the Pd NPs were confined in the ZIF-8 framework during the sacrificial transformation process.

2.3. One-pot method

Compared to the above two strategies, the one-pot method is straightforward that only required to mix the precursor of metal and MOFs, then a self-assembly process is conducted to generate metal species@MOFs composites. Though the one-pot method is easy to operate and ease of mass production, the controlling of sizes, shapes, compositions and uniformity of the confined metal

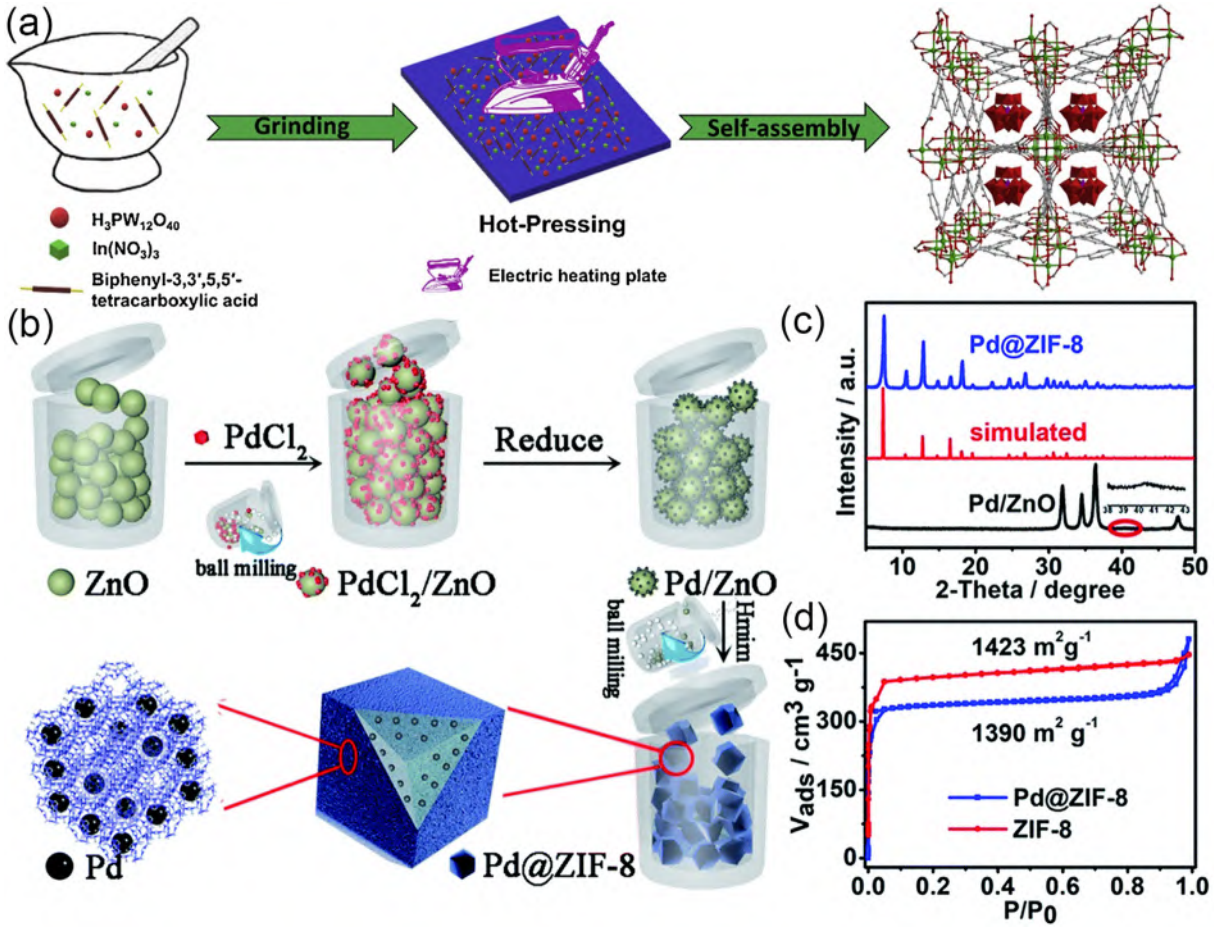

Fig. 5. (a) The hot-pressing synthesis process of PW_{12}@MFM-300(In) Reproduced with permission [63]. Copyright 2019, Elsevier; (b) XRD patterns of Pd/ZnO and Pd@ZIF-8; (c) N_2 adsorption-desorption isotherms of ZIF-8 and Pd@ZIF-8 at 77 K. Reproduced with permission [69]. Copyright 2019, Royal Society of Chemistry.

species in MOFs is hard as the heterogeneous nucleation and growth of MOFs around NPs requires the specific conditions [70].

By controlling the formation of MOFs and metal species, the metal species can be confined in MOFs through the one-pot method. N, N-dimethylformamide (DMF) is a widely used solvent in the fabrication of MOFs, while it can serve as a mild reducing agent for reducing the metal ions and stabilizing the obtained metal species [71]. Based on the hard-soft acid-base (HSAB) principle, the soft C–N group in DMF may priorly adsorb on metal species surface while the C = O group in DMF can have an interaction with the hard oxophilic metal cation of MOFs, which can link the metal species and MOFs precursors that causing prior anisotropic growing of MOFs around metal species instead of self- nucleation. Li et al. [72] found that most of the Pt NPs were not well confined in UiO-66 when mixed H_2PtCl_6 and UiO-66 precursors in DMF directly, as the slower formation rate of Pt NPs compared to UiO-66 (Fig. 6a, top). The kinetically modulated one-pot method that applied acetic acid to reduce the formation rate of UiO-66 and/or H_2 to accelerate the reduction rate of Pt NPs, which can achieve the even and controllable confinement of Pt NPs in UiO-66 (Fig. 6a, down). In the synthetic process, the H_2PtCl_6 and UiO-66 precursors were mixed in DMF with the existence of acetic acid under the H_2/air atmosphere. With H_2 and DMF as the reducing agent, the H_2PtCl_6 was rapidly transformed to Pt NPs at the synthetic temperature of UiO-66. Then, UiO-66 was spontaneously grown around Pt NPs based on the HSAB principle. The porous UiO-66 can limit the overgrowth and aggregation of the confined Pt NPs. TEM images showed Pt NPs were slightly aggregated without H_2 treatment (Fig. 6b), while the Pt NPs with the particle size of 1.7 ± 0.3 nm was confined in UiO-66 with 1:2 H_2/air ratio (Fig. 6c). As the H_2/air ratio increased, the Pt-free UiO-66 shell was thicker (Fig. 6d,e and g), while Pt NPs size remained almost unchanged and the Pt NPs were highly dispersed. In comparison, Pt/UiO-66 was fabricated by the impregnation method, obvious aggregation of Pt NPs was presented as the diffusion resistance made most of Pt NPs were loaded on the outer surface of UiO-66 (Fig. 6f). Moreover, by controlling the nucleation rate of UiO-66, the Pt-free UiO-66 shell also can be modulated (Fig. 6h–m).

Particularly, the confinement of metal precursors via linker design prior to MOFs assembly is effective for capturing the metal precursors and stabilizing the in-situ generated metal species and for promoting the hetero-nucleation of MOFs around metal species [73]. Chen et al. [74] applied 2, 2′-bipyride − 5, 5′-dicarboxylic acid for anchoring the Pd ions and partly displaced the biphenyldicarboxylic acid (H_2bpdc, the organic linker of UiO-67). The confinement of Pd precursors via linker design prior to UiO-67 assembling and followed by H_2 reduction, which resulted in the uniform distribution of Pd NPs in the pores of UiO-67. Furthermore, Li et al. [75] found this method can be applied in preparing non-noble metal Ni NPs and PdNi alloy confined in UiO-67.

In addition, the one-pot method can be carried out through temperature control without an extra reducing agent, where the in-situ Pd precursor incorporation (80 °C) and on-site moderate reduction (130 °C) to induce the reducibility of DMF to generate Pd NPs (Fig. 6n) was conducted [76]. The $PdCl_2(CH_3CN)_2$ was mixed with the UiO-67 precursor in DMF and stirred at 80 °C.

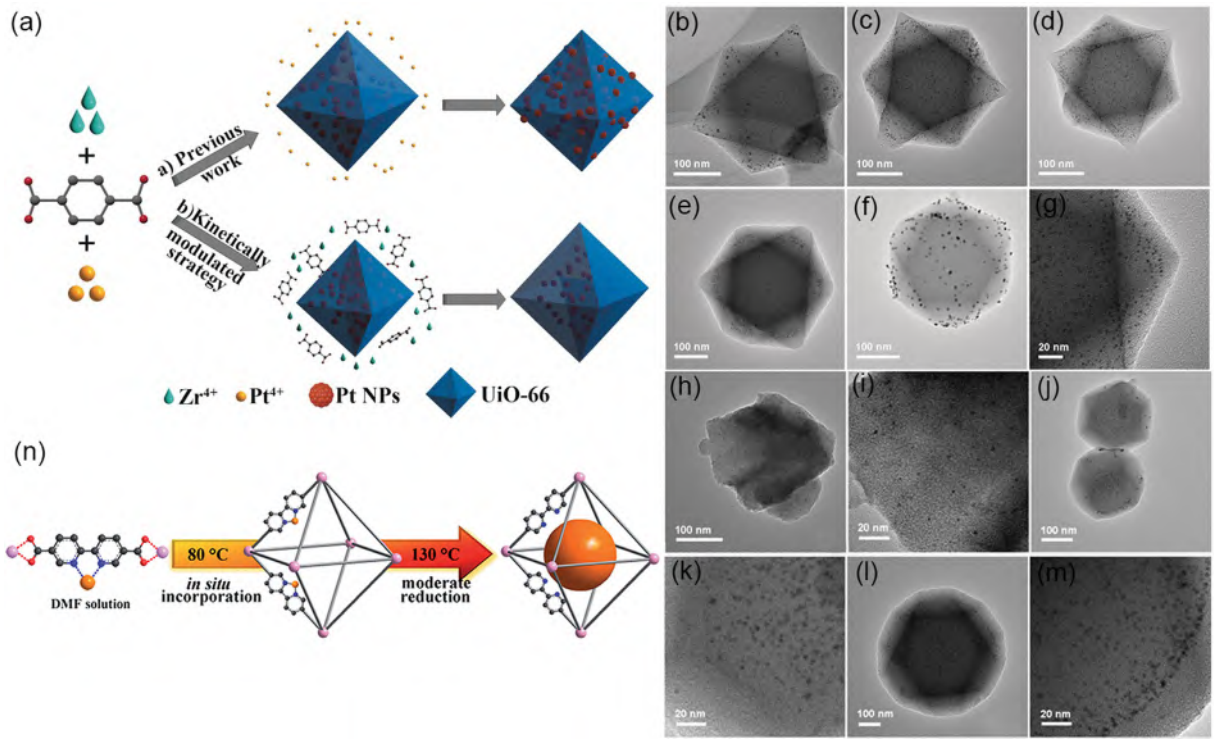

Fig. 6. (a) Incorporation of Pt NPs in MOFs through an in-situ one-step strategy (top) and a kinetically modulated in situ one-step strategy (down); TEM images of Pt@UiO-66 nanocomposites prepared in the presence of H_2/air with a volume ratio of 0:1 (b), 1:2 (c), 1:1 (d, g), and 2:1 (e); TEM image of Pt/UiO-66 prepared by impregnation (f); TEM images of Pt@UiO-66 nanocomposites prepared in the presence of 0 (h, i), 60 (j, k), and 90 (l, m) equivalents of acetic acid. Reproduced with permission [72]. Copyright 2016, Wiley; (n) One-step encapsulation of Pd NPs inside UiO-67 via a temperature control program. Reproduced with permission [76]. Copyright 2015, Royal Society of Chemistry.

Subsequently, the temperature was raised to 130 °C to generate Pd-in-UiO-67. When the temperature was raised, the color of products changed from light-yellow to dark, suggesting Pd^{II} was transformed to Pd^0, the solvent DMF can also serve as reducing agent for generation of Pd NPs as DMF can easily infiltrate the internal space of UiO-67 because of its lipophilic property.

2.4. Self-sacrifice method

The precisely arranged metal sites in MOFs make it possible to in-situ transformed the partial metal sites into metal species and confined in the MOFs. The partial thermal decomposition of MOFs is simple for fabricating metal species@MOFs without the adding of the additional metal precursors and protecting surfactants. The appropriate decomposition temperature is vital as the excessive temperature resulted in the structural collapse of MOFs while the metal species cannot be generated at low temperature. Mukoyoshi [77] reported a partial thermal decomposition of Ni-MOF-74 (Ni_2(dhtp), H_4dhtp = 2,5-dihydroxyterephthalic acid) to fabricate Ni NPs confined in Ni-MOF-74 with nanoscale size (from 2.0 nm to 5.0 nm), the size can be adjusted by changing the heating temperature and time (Fig. 7a). They heated the Ni-MOF-74 to 250–350 °C under vacuum and obtained a series of Ni NPs confined in Ni-MOF-74 (Ni NP@MOF-74). Fig. 7b showed the products heated at 300 °C for 12 h (300–12 h) displayed similar characteristic peaks to Ni-MOF-74, while broad peaks belonged to Ni lattice were observed by elevating temperature to 350 °C for 12 h (350–12 h). However, when heated at 400 °C (400–12 h), the characteristic peaks belonged to the pristine Ni-MOF-74 disappeared, while a Ni pattern was exhibited. The composition of Ni NP@Ni-MOF-74 was expected to be $Ni_2(C_8O_6H_2)\bullet 9H_2O\bullet 5Ni\bullet 6C$ and a part of the organic linker decomposed into volatile matters. Fig. 7c showed the highly dispersed NPs were found throughout the Ni-MOF-74 with an average size of 4.3 ± 1.4 nm. Additionally, electron diffraction peaks belonging to (111), (002) and (022) planes of the Ni NPs were showed (Fig. 7c inset).

Cao et al. [78] applied conductive Cu-based CuHHTP (2, 3, 6, 7, 10, 11-hexahydroxytriphenylene (HHTP)) with uniformly distributed Cu-O_4 nodes to in-situ generate Cu_2O through a simple electrochemical method (Fig. 7d). During the electroreduction process at −1.2 V vs. RHE for 30 min, a part of unstable Cu ions in CuHHTP were reduced and confined in the remained MOFs to fabricate Cu_2O@CuHHTP. The XRD pattern of Cu_2O@CuHHTP in Fig. 7e showed the existence of the characteristic peaks of CuHHTP while a new peak belonged to the (111) plane Cu_2O was performed. Cu 2p XPS spectrum in Fig. 7f displayed that both CuHHTP and Cu_2O@CuHHTP possessed a peak of 934.4 eV which belonged to Cu^{2+} species, implying a part of Cu ions were coordinated to HHTP after electroreduction treatment. Compared to CuHHTP, the peak at 933.1 eV attributed to the Cu^+ or Cu^0 species was showed in Cu_2O@CuHHTP, indicating partial Cu^{2+} ions were reduced. Synchrotron-based X-ray absorption spectroscopy (XAS) was applied to explore the type of Cu species. The X-ray absorption near edge structure (XANES) spectra of Cu K-edge (Fig. 7g) performed the existence of a new peak at 8982.1 eV belonged to Cu^+ species in Cu_2O@CuHHTP compared to CuHHTP, suggesting partial Cu^{2+} ions were transferred to Cu_2O. The extended X-ray absorption fine structure (EXAFS) spectra (Fig. 7h) showed a strong peak at 1.5 Å corresponding to Cu–O scattering was presented in CuHHTP and Cu_2O@CuHHTP, while no Cu-Cu peak at 2.21 Å was exhibited in Cu_2O@CuHHTP, thus no Cu NPs were formed. Moreover, the XANES spectra curve and EXAFS spectra curve of Cu_2O@CuHHTP and CuHHTP were similar, indicating the major structure of CuHHTP was retained. TEM images showed no other NPs were existed in CuHHTP (Fig. 7i), while plentiful NPs with a mean size of 3.5 nm were formed in Cu_2O@CuHHTP with high dispersion (Fig. 7j) [78].

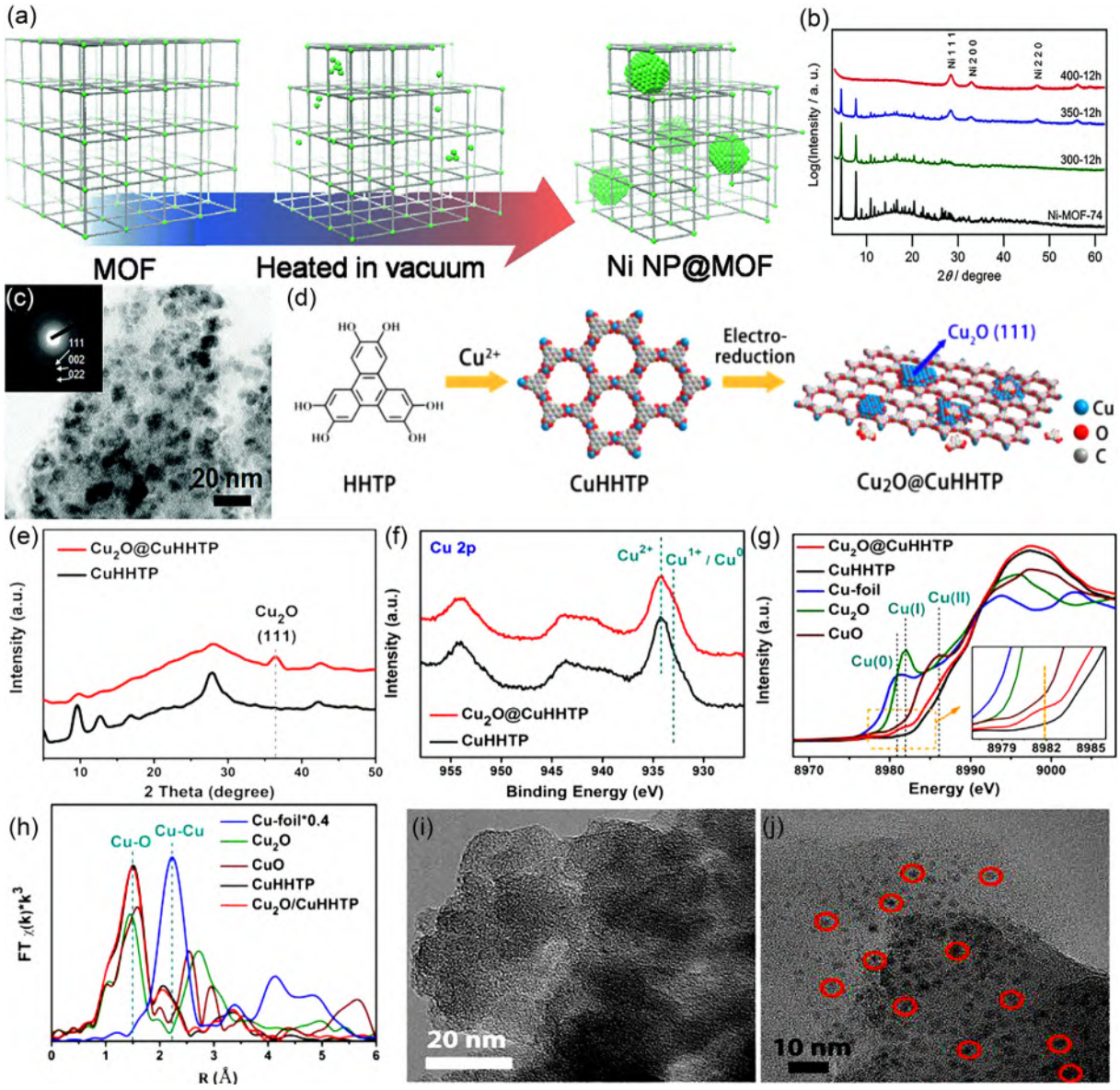

Fig. 7. (a) Scheme of the synthesis of Ni NPs@MOF; (b) Powder XRD patterns of Ni-MOF-74, 300-12h, 350-12h and 400-12h; (c) TEM image of 350-12h with electron diffraction (inset). Reproduced with permission [77]. Copyright 2015, Royal Society of Chemistry. (d) Schematic diagram of the solvothermal synthesis of CuHHTP and preparation of Cu_2O@CuHHTP via electrochemical treatment; (e) XRD patterns and (f) Cu 2p XPS spectra of CuHHTP and Cu_2O@CuHHTP; (g) Normalized Cu K-edge XANES spectra and (h) Fourier transform EXAFS spectra of the Cu-based samples; TEM image of CuHHTP (i) and (j) Cu_2O@CuHHTP. Reproduced with permission [78]. Copyright 2020, Wiley.

3. Location characterization

MOFs with highly ordered porous structure and well-defined chemical functionality provide inherent conditions to confine metal species as well as precise characterization of the composite. The location of metal species relative to MOFs is generally based on the size of metal species and MOFs pores. When the size of metal species is smaller than MOFs, the metal species may be embedded into the pores of MOFs. On the contrary, it may be loaded on the outer surface of MOFs [79]. It is worth noting that the advanced characterizations should be utilized to investigate the location of metal species relative to the MOFs.

Transmission electron microscopy (TEM) can characterize the morphology and size of metal species. Generally, TEM characterization can preliminarily estimate the relative location of metal species by comparing the particle size of metal species and the pore size of MOFs [80]. Recently, surface area and the pore size measured by N_2 adsorption–desorption characterization has been regarded as an important characterization to estimate whether the metal species are confined in MOFs for the confined metal species in the pores might block some pores of MOFs and decrease the surface area as compared to the pristine MOFs. However, it does not exclude the case that the metal species agglomerated on the external of MOFs that result in the overall active surface area [30]. Therefore, more accurate and advanced characterizations should be applied.

Single crystal X-ray diffraction is effective to determine the chemical composition and structure of a crystalline material. In the last decades, with the development of synchrotron radiation, the single crystal synchrotron X-ray diffraction has achieved more precise Bragg diffraction data, as the variable photon energy and much higher flux can decrease systematic errors caused by absorp-

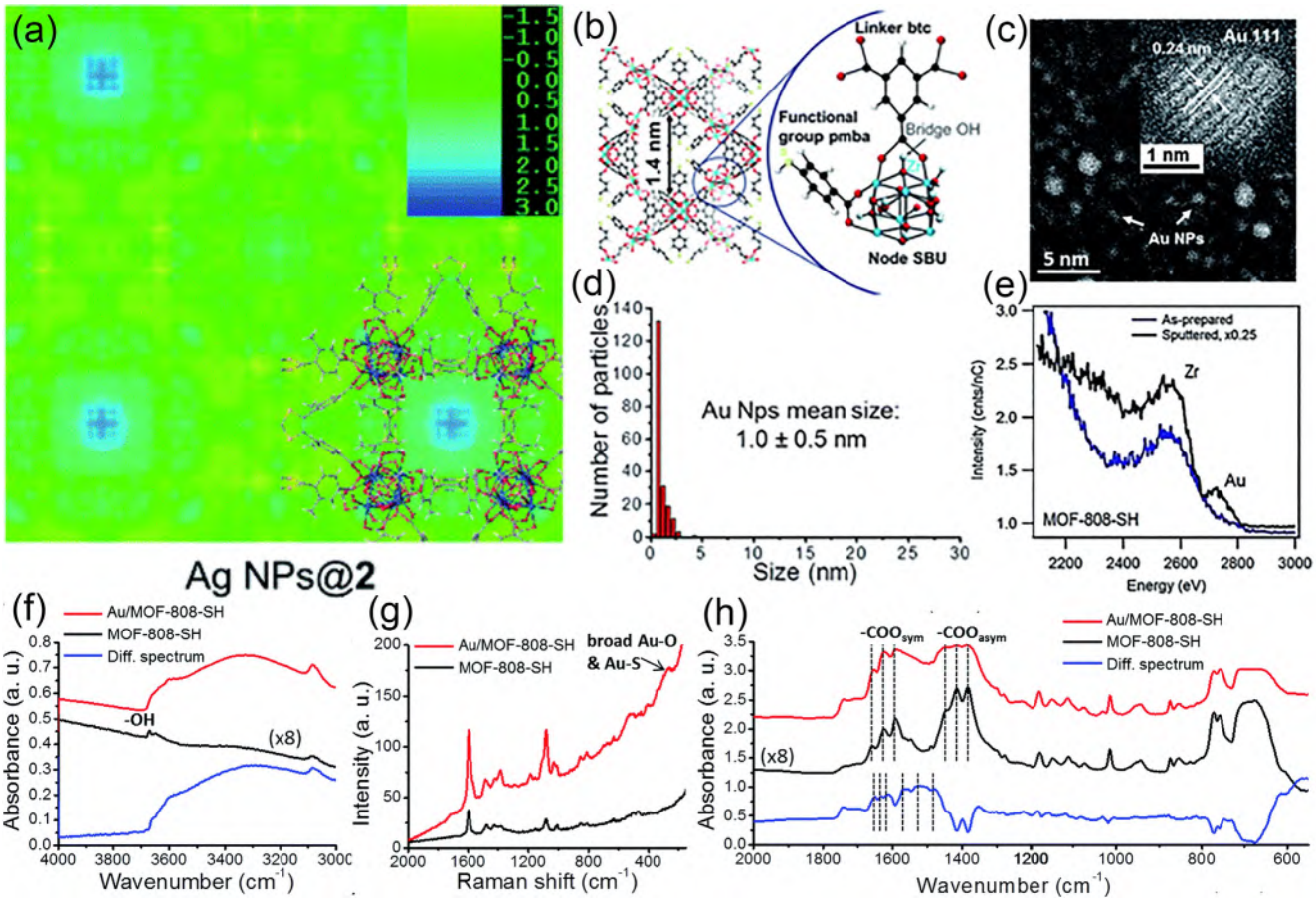

Fig. 8. Electron density (ED) map for Ag NPs**@2** single crystal structure (a) Reproduced with permission [48]. Copyright 2020, Royal Society of Chemistry; structure of MOF-808-SH (b), HRTEM observation of the Au/MOF-808-SH (the inserted Figure was crystalline Au NPs) (c), Au NPs size distribution of Au/MOF-808-SH (d) and LEIS spectra of Au/MOF-808-SH before and after sputtering (4×10^{14} cm^{-2} Ar^+ ions) (e), Infrared spectra of the 4000–3000 cm^{-1} region (f) and 2000-550 cm^{-1} region (g), differential spectra was described as blue, Raman spectra (h). Reproduced with permission [83]. Copyright 2019, Royal Society of Chemistry. (For interpretation of the references to colour in this figure legend, the reader is referred to the web version of this article.)

tion, extinction and anomalous scattering [81,82]. For instance, the electron density map of Ag NPs@2 displayed a strong residual electron density at the center of the small cavity, indicating the reduced Ag NPs were confined in the cavities of compound 2 [48].

Cure et al. [83] found that the average size of Au NPs (1.0 ± 0.5 nm) in Au/MOF-808-SH (Fig. 8c and d) matched well with the pore size of MOF-808–SH (1.07 ± 0.05 nm), which proved the Au NPs confined inside the thiol groups functionalized MOF-808. However, when attached $–NH_2$ groups in MOF-808, the average size of Au NPs of Au/MOF-808-NH_2 was 7.1 ± 3.6 nm and no confinement of Au NPs while the $[Zr_6O_4(OH)_4]$ nodes and functional groups were identical to MOF-808–SH (the structure of MOF-808-SH was shown in Fig. 8b). The choose the appropriate functional groups were essential in the confined strategy as $–NH_2$ groups were less soft than -SH groups in HSAB principle. Moreover, they used low energy ion scattering (LEIS) to verify the conclusion. LEIS was a characterization that used inert gas as an ion beam to obtained the atomic composition of the external surface (<1 nm) and provided depth profiling of the external *ca.* 10 nm of the surface [84]. LEIS can distinguish whether the Au NPs on MOF-808-SH surface or confined in its interior. As performed in Fig. 8e, there were strong Zr peaks on Au/MOF-808-SH surface. When concentrated on Au peaks, there was no Au peak on Au/MOF-808-SH surface while Au peak appeared when sputtered with 4×10^{14} cm^{-2} of 8 keV Ar^+ ions. Therefore, the Au NPs were located under the MOF-808-SH surface. Compared to the surface spectroscopies and TEM, optical spectroscopy like infrared (IR) and Raman spectra can detect the interactions between Au NP and ligands. As IR spectra (Fig. 8f and g) displayed, the narrow bands at 3671 cm^{-1} of MOF-808-SH were belonged to the stretch of the four bridge O–H groups while they disappeared in Au/MOF-808-SH as the direct bonding of Au to O. Raman spectra (Fig. 8h) confirmed the IR results that show sharp modes at 262 and 259 cm^{-1} in MOF-808, MOF-808-SH, respectively, which were identified as Au-O bonding.

In addition, various advanced methods can be utilized to examine the structure of materials, while some are novel and not yet widely utilized in characterizing the relative location of metal species and MOFs. Take the researches of Jiang et al as an example. X-ray absorption spectroscopy (XAS) characterization can obtain the structure information and electronic states on the atomic scale. They stabilized ultrafine Au NPs with an average atom number of 2.5 in the pores of Cd-based MOFs (Au-1) [85]. The Cd-based MOF was prepared of $Cd(NO_3)_2{\cdot}6H_2O$ with 4,4′-(hexafluoroisopropylidene) diphthalate (L), in $EtOH/H_2O$ to produce $[Cd_2(L)(H_2O)]\bullet 0{\cdot}.5H_2O$ (1) (The coordination environment of 1 were performed in Fig. 9a–d). Fourier transform magnitude of extended X-ray absorption fine structure (FT-EXAFS) spectrum of the Au-1 showed the existence of Au-Au, Au-F or Au-O interactions (Fig. 9e), which demonstrated the ultrafine Au clusters confined in the fluoro-coated channels of MOFs. When involved in the metal species

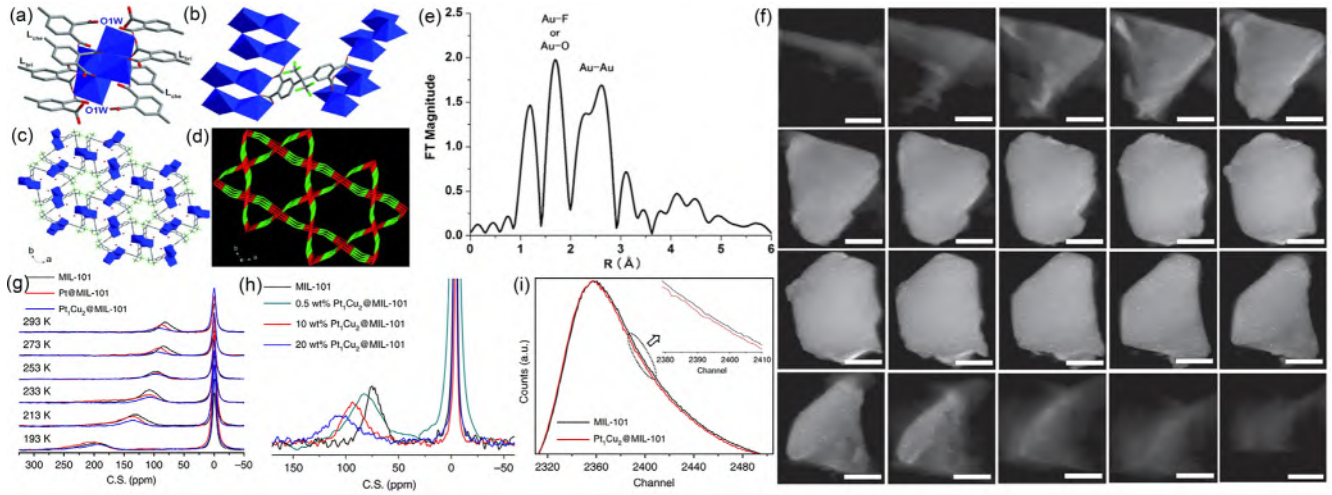

Fig. 9. View of the coordination environments of 1: the Cd_4 cluster connected by eight L (a); L connected by four metal clusters (b); View (c) and topological view (d) of the 3D network of 1 (blue Cd, red O, green F, gray C); Au L_{III}-edge FT-EXAFS spectrum for Au-1 (e). Reproduced with permission [85]. Copyright 2011, Wiley. Reconstructed slice images: Selected reconstructed slice images (observed in the order of left to right and top to down) throughout the entire Pt_1Cu_2@MIL-101 skeleton. The scale bar on the images is roughly ~200 nm (f); Temperature-dependent hyperpolarized 129Xe NMR spectra for MIL-101, Pt@MIL-101, and PtCu@MIL-101. The measurements were performed in the range of 193–293 K (g); Hyperpolarized 129Xe NMR spectra performed at 293 K for MIL-101, and Pt_1Cu_2@MIL-101 with various metal percentages (h); Positron lifetime spectra for MIL-101 and 0.5 wt% Pt_1Cu_2@MIL-101 based on positron annihilation experiments (i). Reproduced with permission [79]. Copyright 2019, Nature. (For interpretation of the references to colour in this figure legend, the reader is referred to the web version of this article.)

consisted of tens or even hundreds of atoms, other reliable characterizations were needed. Recently, Jiang et al. encapsulated monometallic Pt (1.5 nm) and bimetallic PtCu NPs (1.7 nm) into MIL-101(Cr) [79]. First, they utilized TEM and controlled HAADF-STEM at consecutive tilt angles from −62.6° to 62.6° and observed the size of Pt NPs or PtCu NPs were smaller than the pores and the metal species were confined in the pores of MIL-101(Cr) with high dispersion. Tomographic slices measurement observed the PtCu NPs were highly dispersed throughout the whole MIL-101 crystal (Fig. 9f). To further verify the above judgment, hyperpolarized ^{129}Xe NMR spectroscopy was applied as the ^{129}Xe molecule can easily go through the pores and its highly polarized electron cloud was sensitive to the guest metal species in the pores, which can be used to investigate the porosity characterization of MOFs [86,87]. As Fig. 9g showed, the peaks at 0 ppm were owing to the free ^{129}Xe gas, the signals at the lower field were attributed to the interactions between Xe molecules and guest metal species. As the temperature decreased, the ^{129}Xe chemical shifts increased for the increased Xe-Xe interactions Xe–Xe interactions. Moreover, the ^{129}Xe chemical shifts of samples followed the order: MIL-101 < P t@MIL-101 < PtCu@MIL-101. The lower Xe concentration brought a larger chemical shift, thus the Pt NPs and PtCu NPs mainly confined in MIL-101 and the size of PtCu NPs was larger than Pt which confirmed the TEM results. Moreover, hyperpolarized 129Xe NMR spectra were tested at a constant temperature (293 K). As Fig. 9h showed, Xe chemical shifts increased as the increased metal percentage from 0.5 wt% to 20 wt% of PtCu NPs in PtCu@MIL-101 which further confirmed the metal species were mainly confined in MIL-101 pores. Positron annihilation spectrometry (PAS) is a powerful analytical method to investigate the microstructure by measuring the lifetime of the positron (e^+) emitted by a nuclear decay [88]. Obviously, PAS can further confirm the location of metal species for the guest metal species in the channels can effectively capture positrons. Fig. 9i indicated that after confining of PtCu NPs, the free space in the pores of MIL-101 was smaller and the long lifetime component decreased. Therefore, the above characterizations can effectively prove the location of metal species relative to MOFs.

4. Photocatalytic applications

During the photocatalytic process, the photocatalyst is irradiated by sunlight, when the photons with energy higher than the energy gap (Eg) of photocatalyst, charge transfer will occur. In general, the photo-generated electrons (e^-) and holes (h^+) formed from the highest occupied molecular orbitals (HOMO) to the lowest unoccupied molecular orbitals (LUMO) in MOFs-based photocatalyst [89]. The strongly oxidizing holes and highly reductive electrons will be involved in the photocatalytic reactions. In addition, bulk or surface recombination will be occurred to decrease the photocatalytic efficiency [90,91].

The key to the photocatalytic technology is the fabrication of photocatalyst [92]. The porous structure of metal species@MOFs enables the exposure of active sites as much as possible and promote the access of substrates to active surface by improving mass-transfer efficiency and decreasing the transfer time between catalytic centers [93]. The confinement of MOFs can promote the substrate–catalyst interactions [94]. Moreover, due to the interface effect and size effect [95], the confined metal species are highly dispersed and can boost the intrinsic photocatalytic performance. For example, Li et al. [96] found that the cavity-confined Pd NPs contained more active unsaturated Pd atoms than Pd NPs loaded on MIL-100(Fe) surface due to their small size and high dispersion. The encapsulation of photoactive metal species to harvest sunlight can better transmit the absorbed energy to the organic ligand of MOFs, which is a key aspect to fabricate photocatalyst with high performance. When the noble metals like Ag, Au NPs are irradiated, the photo-generated electrons in conduction band (CB) are oscillated coherently, which is considered as surface plasmon resonance (SPR) and greatly improved the light adsorption [97]. SPR is a quasi-particle of free electrons and electromagnetic resonance quantization, which can significantly increase the interaction between light and the metal species. Importantly, the incident light is concentrated on metal species surface and greatly improved light adsorption [98].

The optical characterizations and electrochemical analysis can be used to obtain the information on the intrinsic properties of

photocatalysts and photo-generated carriers in photocatalytic process. Recently, density functional theory (DFT) calculation has become a powerful tool to explore the effects of charge distribution, adsorption energies, electronic structure, or even defect states on the photocatalytic reaction [99]. Next, we will concentrate on presenting the progress in photocatalytic applications of H_2 production, CO_2 reduction and water remediation using metal species@MOFs, the corresponding photocatalytic mechanism are also discussed.

4.1. Hydrogen production

Hydrogen (H_2) production from water splitting can be an ideal candidate for decreasing the use of fossil fuel as the gravimetric energy density of H_2 (up to142 MJ kJ mol^{-1}) is almost three times that of gasoline [100]. In the reaction, the photocatalyst can be excited by light irradiation and generated photogenerated electrons and holes for reducing and oxidizing water to produce H_2 without the generation of side-products. To ensure the H_2 generation, the energy-band location of the photocatalyst is important. The LUMO should be more negative than the reduction potential of H^+/H_2 (0 V vs normal hydrogen electrode (NHE)), while the HOMO is more positive than the oxidation potential of O_2/H_2O (+1.23 V) [101]. Due to the photogenerated H_2 can react with O_2 to produce H_2O, the amount of H_2 emitted will be reduced. Therefore, the addition of sacrificial reagents as electron scavengers like methanol, ethylene diamine tetraacetic acid (EDTA), triethanolamine (TEOA), $AgNO_3$ into the photocatalytic reaction can act as outer driving force for the surface chemical reaction and restrain the H_2O production [102,103]. Generally, the photocatalytic hydrogen generation activity can be estimated by photocatalytic hydrogen generation (Eq. (1)), apparent quantum efficiency (AQE, Eq. (2)) and turnover efficiency (TOF, Eq. (3)).

$$\textit{Photocatalytic hydrogen generation activity} = \frac{\textit{hydrogen gas evolution}}{\textit{amount of photocatalyst} \times \textit{illumination time}} \tag{1}$$

$$\textit{Apparent quantum efficiency} = \frac{\textit{number of reacted electrons}}{\textit{number of incident photons}} \times 100\% = \frac{2 \times \textit{number of resultant } H_2 \textit{ molecules}}{\textit{number of incident photons}} \times 100\% \tag{2}$$

$$\textit{Turnover efficiency} = \frac{\textit{Moles of } H_2 \textit{ evolved in 1h}}{\textit{Moles of catalyst}} \tag{3}$$

The confined strategy of metal species in MOFs pores can greatly enhance the separation efficiency and utilization of photogenerated charge-carriers. Jiang et al. [104] compared the photocatalytic hydrogen generation activity of Pt NPs with a diameter of 3 nm confined inside or loaded on UiO-66-NH_2, named as

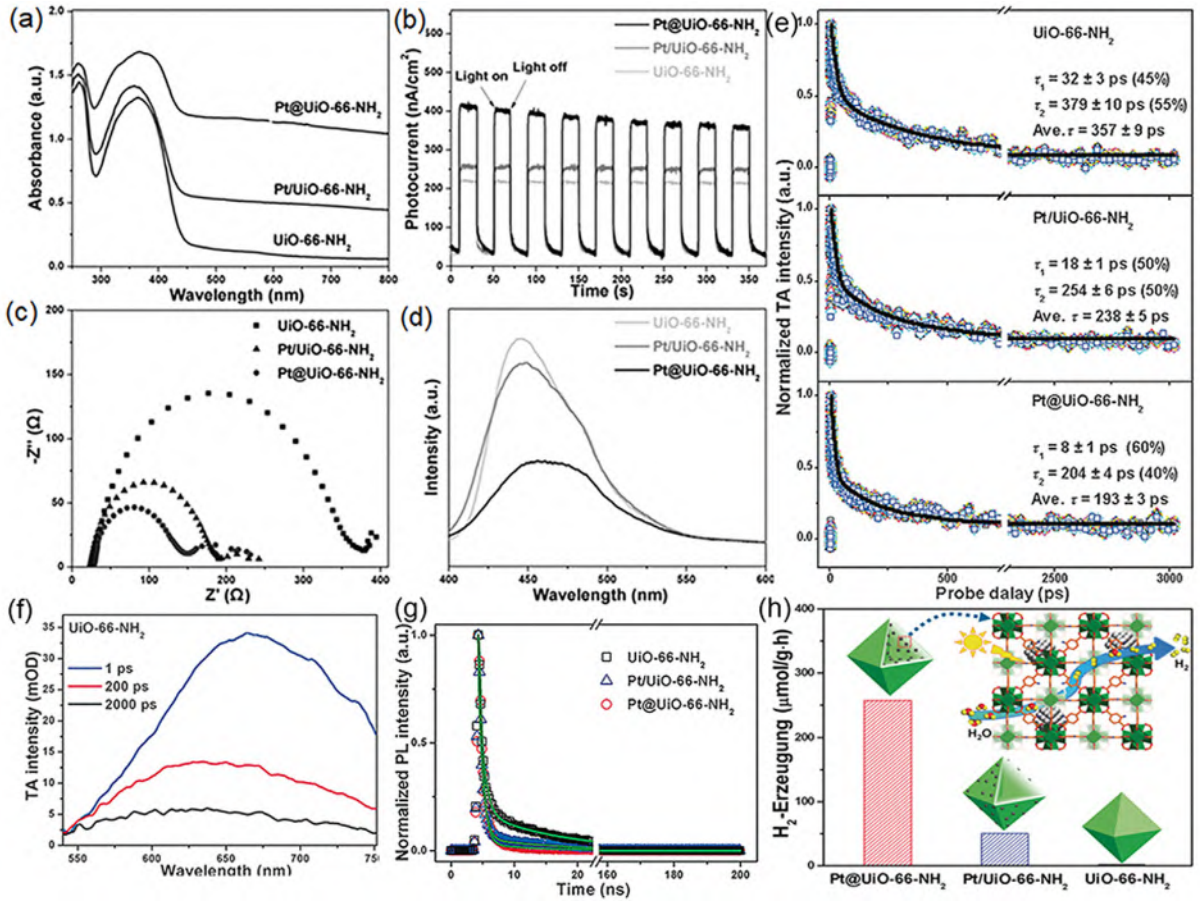

Fig. 10. (a) UV/Vis diffuse reflectance spectra; (b) photocurrent responses; (c) EIS Nyquist plots; (d) PL emission spectra (excited at 400 nm) for UiO-66-NH_2, Pt@UiO-66- NH_2, and Pt/UiO-66-NH_2; (e) TA kinetics; (f) TA spectra of UiO-66-NH_2 (excitation at 400 nm) with TA signal given in mOD (OD: optical density); (g) Time-resolved PL decay profiles for UiO-66-NH_2, Pt@UiO-66-NH_2, and Pt/UiO-66-NH_2, respectively (lex = 400 nm, lem = 455 nm) and (h) the H_2 production rate of Pb@UiO-66-NH_2, Pt/UiO-66-NH_2, UiO-66-NH_2 and the photocatalytic hydrogen production process over Pb@UiO-66-NH_2. Reproduced with permission [104]. Copyright 2016, Wiley.

Pt@UiO-66-NH_2 and Pt/UiO-66-NH_2, respectively. The H_2 production was carried out with TEOA in CH_3CN. Compared to the pristine UiO-66-NH_2 (1.72 μmol $g^{-1}h^{-1}$), both Pt@UiO-66-NH_2 and Pt/UiO-66-NH_2 showed enhanced hydrogen-production activities while the Pt@UiO-66-NH_2 (257.38 μmol $g^{-1}h^{-1}$) exhibited much higher efficiency than Pt/UiO-66-NH_2 (50.26 μmol $g^{-1}h^{-1}$) (Fig. 10h). For Pt NPs/UiO-66-NH_2 photocatalysts, Pt NPs with a low overpotential acted as effective electron traps for the transformation of photogenerated electrons from UiO-66-NH_2 to Pt NPs through the Schottky junction. Obviously, the Pt@UiO-66-NH_2 greatly shortened the electron-transport distance and restrained the electron-hole recombination for the Pt NPs confined in UiO-66-NH_2 were accessible to protons. The UV/Vis diffuse reflectance spectra (Fig. 10a) showed stronger absorption than Pt/UiO-66-NH_2 and UiO-66-NH_2 in visible region, the close packing between Pt NPs and UiO-66-NH_2 may result in higher scattering at long wavelengths. Photocurrent (Fig. 10b), electrochemical impedance spectroscopy (EIS, Fig. 10c) and photoluminescence (PL) emission spectroscopy (Fig. 10d) manifested the highest separation and transformation efficiency and the lowest recombination efficiency of photogenerated electron-hole pairs in Pt@UiO-66-NH_2. Furthermore, Pt@UiO-66-NH_2 exhibited acceleration of transient absorption (TA) decay kinetics (Fig. 10e and f) and decrease of PL lifetime (Fig.10g), further confirming more efficient charge separation and transformation in Pt@UiO-66-NH_2. Moreover, the Pt NPs confined in UiO-66-NH_2 may not result in aggregation or leaching of Pt after photocatalytic process, thus Pt@UiO-66-NH_2 exhibited high recyclability and stability.

It is convenient to introduce specific groups in MOFs due to their structural diversity. Su et al. fabricated highly dispersed Pt NPs of 3 nm confined in Pd-PMOF-2(Hf) and exhibited excellent H_2 production activity, which achieved a maximum H_2 generation rate of 22 674 μmol $g^{-1}h^{-1}$ with using TEOA as a sacrificial agent [105]. The synergistic effect between Pt NPs and Pd-PCN-222(Hf) accelerated the photocatalytic hydrogen generation: (a) the Pd-porphyrin ligands with long-lived room temperature phosphorescence were uniformly distributed in Pd-PCN-222(Hf), which contributed to an extensive light absorption without mutual electron coupling quenching; (b) the well-confined Pt NPs can form Schottky barrier with Pd-porphyrin ligand to facilitate the separation and transfer of photo-generated carriers; (c) The hydrophilic Hf-O clusters with carboxylate linkers in Pd-PMOF-222(Hf) shell enhanced chemical stability and brought water concentration effect; (d) the Pt@Pd-PCN-222 (Hf) composite avoided Pt NPs aggregation, making for the charge transfer between Pd-porphyrin and Pt-NPs and improved the stability of composites.

It is well known that the noble metals (such as Pt, Pd) are promising cocatalysts towards photocatalytic hydrogen generation. Other non-noble metal species are also reported to show great photocatalytic performance [106]. Jiang et al. [107] confined transition metal phosphides (Ni_2P, $Ni_{12}P_5$) and Pt NPs with similar sizes (around 10 nm) in UiO-66-NH_2, which named as Ni_2P@UiO-66-NH_2, $Ni_{12}P_5$@UiO-66-NH_2 and Pt@UiO-66-NH_2, respectively. Notably, the UiO-66-NH_2 showed negligible H_2 production rate (2.1 μmol·g^{-1}·h^{-1}) under visible-light irradiation, while $Ni_{12}P_5$@-UiO-66-NH_2, Ni_2P@UiO-66-NH_2 and Pt@UiO-66-NH_2 exhibited H_2 production rate of 293.2 μmol·g^{-1}·h^{-1}, 409.1 g^{-1}·$h^{-1}$and 378.0 μmol·g^{-1}·h^{-1}, respectively (Fig. 11a). Linear sweep voltammetry (LSV) showed the Pt@UiO-66-NH_2 with the lowest overpotential, indicating the Pt NPs was thermodynamically favourable to Ni_2P and $Ni_{12}P_5$ (Fig. 11b). Steady-state photoluminescence (PL) spectra showed the peak intensity around 450 nm followed: Ni_2P@UiO-66-NH_2 < Pt@UiO-66-NH_2 < $Ni_{12}P_5$@UiO-66-NH_2 < UiO-66-NH_2 (Fig 11c), the minimum intensity of PL signal in Ni_2P@UiO-66-NH_2 implied the lowest recombination rate of photo-generated electron-hole pairs (Fig. 11d). Photocurrent results displayed the Ni_2P@UiO-66-NH_2 showed the strongest photocurrent response, suggesting the highest separation efficiency of photo-generated electron-hole pairs (Fig. 11e). Moreover, the electrochemical impedance spectroscopy (EIS) images showed the Ni_2P@UiO-66-NH_2 presented the smallest radius, indicating the lowest resistance of interfacial charge transfer. The photoelectrochemical characterization suggested the Ni_2P was kinetically preferred to Pt NPs and $Ni_{12}P_5$ Ni_2P. In addition, the strongest electron spin resonance (ESR) signal (Fig. 11f) and the lowest relaxation lifetime in ultrafast TA spectroscopy (Fig. 11g) suggested the optimum ability of Ni_2P@UiO-66-NH_2 to accelerate link-to-cluster charge transfer (LCCT) process in photocatalytic hydrogen production. Therefore, the highest H_2 production of Ni_2P@UiO-66-NH_2 was a balanced result between thermodynamics and dynamics.

DFT can further illustrate the enhanced photocatalytic activity as the hydrogen binding free energy (ΔG_{H^*}) is related to the

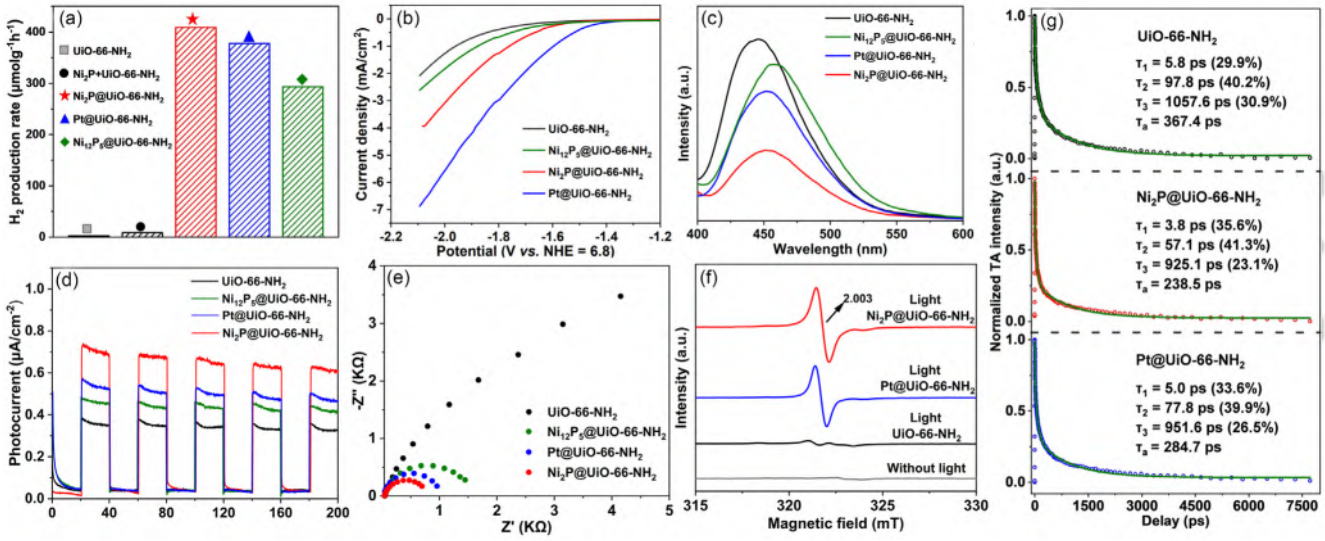

Fig. 11. (a) The photocatalytic hydrogen production rates; (b) LSV curves of samples in 0.1 M Na_2SO_4 aqueous solution (pH = 6.8); (c) PL emission spectra under excitation at 380 nm; (d) photocurrent responses and (e) EIS plots; (f) ESR spectra of UiO-66-NH_2 in dark and UiO-66-NH_2, Pt@UiO-66-NH_2 and Ni_2P@UiO-66-NH_2 under illumination; (g) TA kinetics of UiO-66-NH_2, Ni_2P@UiO-66-NH_2 and Pt@UiO-66-NH_2 near 650 nm and their multi-exponential fits. Reproduced with permission [107]. Copyright 2020, Wiley.

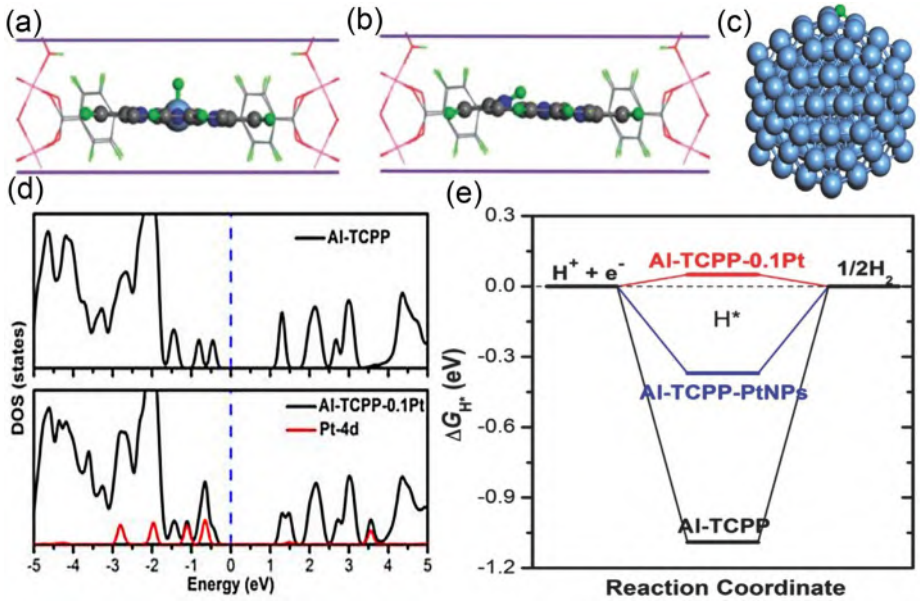

Fig. 12. Geometric structures of H* of (a) Al-TCPP-0.1Pt, (b) Al-TCPP, and (c) Al-TCPP-Pt NPs (Pt_{147}). The sky-blue, grey, red, blue, pink, and green balls represent Pt, C, O, N, Al, and H atoms, respectively; (d) Computed density of states (DOS) of Al-TCPP and Al-TCPP-0.1Pt. The blue dashed lines denote Fermi level (e) Calculated free energy diagram for photocatalytic H_2 production. Reproduced with permission [109]. Copyright 2018, Wiley. (For interpretation of the references to colour in this figure legend, the reader is referred to the web version of this article.)

intrinsic activity of the active site in the catalyst. Theoretically, ΔG_{H^*} value is nearly zero, a rapid proton/electron-transfer process and hydrogen release can be achieved [108]. Through DFT calculations, Jiang et al. [102] found that the single Pt atoms exhibited superb activity with a TOF of 35 h^{-1}, which was about 30 times than that of Pt NPs confined in Al-TCPP. The density of states analysis (Fig. 12f) exhibited that Al-TCPP and Al-TCPP-0.1Pt possessed identical band gap and similar electronic states near the Fermi level, indicating they may have similar light absorption behavior and the single Pt atom in Al-TCPP-0.1Pt contributed to the states of valence band. The ΔG_{H^*} of hole-involved Al-TCPP-0.1Pt (Fig. 11c), Al-TCPP (Fig. 12d) and Al-TCPP (Fig. 12e) were 0.05 eV, −0.37 and −1.09 eV, respectively (Fig. 12g). The efficient electron–proton acceptance of Al-TCPP-0.1Pt was conducive to form H* and fast hydrogen desorption. Thus, the excellent photocatalytic hydrogen production activity of Al-TCPP-0.1Pt may due to the single Pt atom can optimize H binding and electronic properties.

4.2. CO_2 reduction

The consumption of fossil fuels leads to an excessive emission of carbon dioxide (CO_2), which can increase global temperatures through the greenhouse effect [89]. The reduction of CO_2 into high value-added chemicals by sunlight is a very promising pathway to address energy and environmental issues. However, the C = O bond in CO_2 (+805 kJ mol^{-1}) is extremely stable and the CO_2 reduction reaction requires high energy input [89]. Generally, the CO_2 photoreduction process including the adsorption and activation of CO_2 by photocatalysts and water is used for supplying hydrogen sources. Under irradiation, the photocatalyst was excited to form e^- and h^+, then the e^- shift to the catalytic center and reduced the adsorbed CO_2 into hydrocarbons [109]. Since there are many possible reaction paths, various products (such as CO, HCHO, CH_3OH, CH_4, C_2H_4, C_2H_5OH, C_2H_6, and C_3H_7OH) can be obtained and the photocatalyst with excellent selectivity and efficiency is vital in the photocatalytic CO_2 reduction [110,111]. MOFs exhibit excellent CO_2 capture capability which endows CO_2 molecules have more contact with the active sites and MOFs with high specific surface area is conductive to CO_2 molecules diffusion into the pores [112,113]. However, because of the insufficient light adsorption and inefficient utilization of photo-generated charge carriers, the CO_2 photoreduction capability of MOFs is relatively low. The porous and ordered structure of MOFs enabled them to confine metal species and offered a synergetic effect towards effective photocatalytic reaction. The confinement strategy of metal species within MOFs results in close contact of electron-rich metal species to the catalytic centers of MOFs, which can increase the electron density of MOFs and improve the interactions with CO_2 [5,114].

The confined metal species in MOFs can act as electron traps as well as active sites. Chen et al. [115] fabricated ultra-small Ag NPs (<5 nm) confined in Co-ZIF-9. With adding of $[Ru(bpy)_3]Cl_2{\cdot}6H_2O$ (bpy = 4,4′-bipyr-idine) and TEAO, the Ag@Co-ZIF-9 showed improved activity and selectivity for CO_2-to-CO conversion under visible-light irradiation as the reactivity increased more than doubled (about 28.4 μmol CO) and the selectivity improved by around 20% (22.9 μmol H_2). The confined Ag NPs not only facilitated the separation of photogenerated electron-hole pairs through the Schottky junction, but also accelerated the charge transfer and suppressed H_2 evolution as the Ag NPs with Fermi level of 0.4 V can act as great electron acceptors. As the content of Ag NPs increased, CO production improved remarkably while H_2 evolution decreased. When replaced Ag@Co-ZIF-9 with Ag NPs or a physical mixture of Ag NPs and Co-ZIF-9, low catalytic activity and selectivity was achieved. Therefore, only when Ag NPs were confined in Co-ZIF-9 can accelerate CO_2 photoreduction.

The synergistic effect of MOFs and confined metal species facilitates CO_2 adsorption and offers more active sites. Zhen et al. [116] fabricated Ni@MOF-5 with highly uniform dispersion of Ni (41.8%) by impregnation method for photocatalytic CO_2 methanation. At 320 °C, CO_2 conversion was 75.09% and CH_4 selectivity was 100% over Ni@MOF-5. The homogeneous confinement of Ni and high specific surface area of MOF-5 (2961 m^2 g^{-1}) played a significant role in activity enhancement. Moreover, Ni@MOF-5 exhibited high stability and hardly any decrease of catalytic activity after 100 h of CO_2 methanation. Yan et al. [117] confined $[Ni^{II}(bpet)(H_2O)_2]$ (bpet = 1,2-bis((pyridin-2-ylmethyl)thio)ethane) in Ru-UiO-67

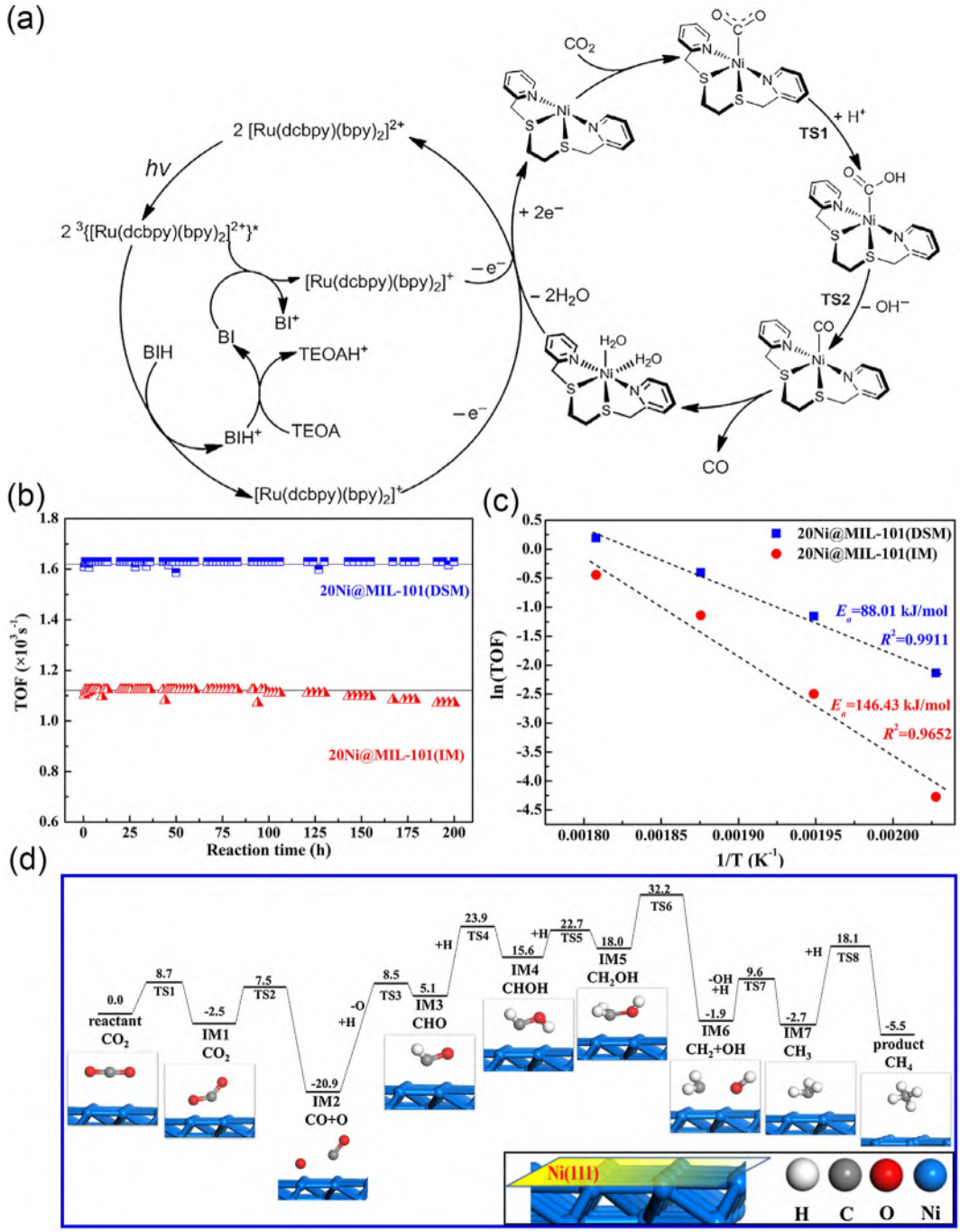

Fig. 13. (a) Proposed mechanism for the photocatalytic reduction of CO_2 to CO in the Ni@Ru-UiO-67/BIH/TEOA system. Reproduced with permission [118]. Copyright 2019, Elsevier. (b) Long-term (200 h) stability tests over 20Ni@MIL-101(DSM) and 20Ni@MIL-101(IM) catalysts at 300 °C; (b) Arrhenius plots for CH_4 TOF over 20Ni@MIL-101(DSM) and 20Ni@MIL-101 (IM) catalysts between 220 °C and 280 °C; (d) Potential energy diagram for CO_2 methanation on the Ni (111) surface slab structure. Each reactant, product and intermediate structures are also shown in the inset of the Figure. The label ''IM'' is the intermediate structure, and ''TS'' is the transition structure. Reproduced with permission [119]. Copyright 2017, Elsevier.

(Ni@Ru-UiO-67) with excellent CO_2 photoreduction activity to obtain CO. As showed in Fig. 13a, under irradiation, the photogenerated electrons were generated through metal-to-ligand charge transfer (MLCT) and then directly transferred to Ni(II) active sites affording Ni^0 for CO_2 reduction. The synergistic effect of Ru-UiO-67 and Ni(II) species accelerated the electron transfer and improved the CO_2 photoreduction. Interestingly, the exposed facet of metal species also has an effect on the photocatalytic activity. Lu et al. [118] synthesized Ni NPs confined in MIL-101 for CO_2 methanation by double solvent method (DSM) and multiple impregnation method (IM). As shown in Fig. 13b, the CH_4 TOF of 20Ni@MIL-101(DSM) was 1.63×10^{-3} s^{-1} (CO_2 conversion: 100%) and CH_4 selectivity was 100% during 200 h reaction while the CH_4 TOF of 20Ni@MIL-101(IM) was comparatively low, about 1.12×10^{-3} s^{-1} before 100 h (CO_2 conversion: 68.9%), and slightly decreased after 100 h. Therefore, 20Ni@MIL-101(DSM) was very stable. According to the activation energies (Ea) calculated by Arrhenius plots (Fig. 13c), the Ea of 20Ni@MIL-101(DSM) and 20Ni@MIL-101(IM) were 88.01 kJ/mol and146.43 kJ/mol, respectively. The lower Ea of 20Ni@MIL-101(DSM) was ascribed to more

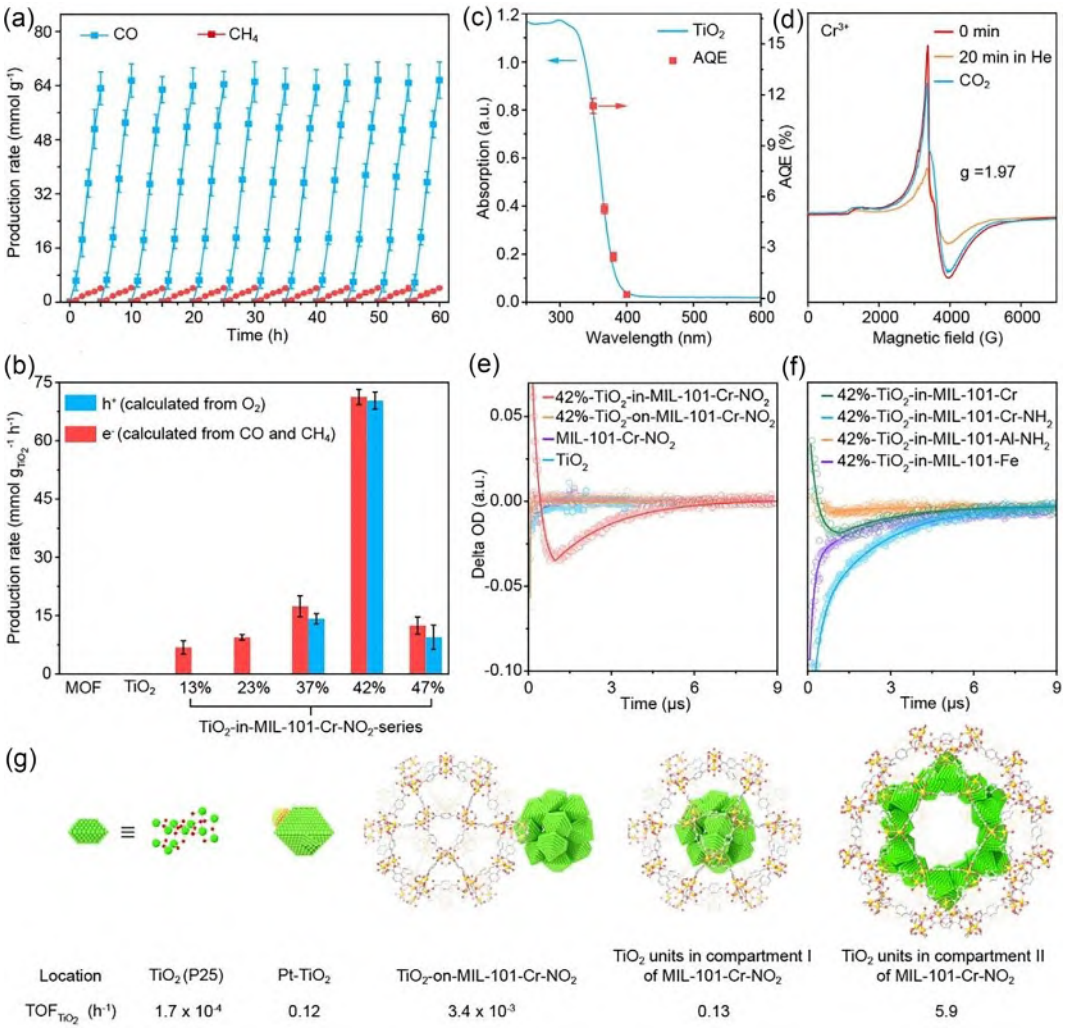

Fig. 14. (a) CO and CH_4 production rate through a 60-hour test using 42%-TiO_2-in-MIL-101-Cr-NO_2 as catalyst (n=3); (b) Equivalent electron and hole production rate of TiO_2-in-MIL-101-Cr-NO_2 series calculated from the reduction and oxidation products, respectively, electrons ($V_{e^-} = 2\times V_{CO} + 8 \times V_{CH4}$) and holes ($V_{h^+} = 4 \times V_{O2}$), (n = 3); (c) AQE of 42%-TiO_2-MIL-101-NO_2 sample at different monochromic light overlaid with light absorption curve of TiO_2 (n = 3); (d) In situ EPR signal of 42%-TiO_2-in-MIL-101-Cr-NO_2 at 2 K in He. The intensity of Cr^{3+} peak changed upon illumination, and followed by CO_2 contact; TAS (λ_{ex} = 355 nm) results of various TiO_2-in-MOF compartments monitored at 380 nm, where the lifetime of excited electrons was derived for TiO_2 (e) and MOFs (f), respectively; (g) Comparison of TOF value per TiO_2 unit for TiO_2 at different locations. Reproduced with permission [120]. Copyright 2020, Nature.

Ni(1 1 1) facet exposed on photocatalyst surface. According to DFT calculations, the Ni (1 1 1) plane had a lower potential energy barrier (10.0 kcal/mol) for CO_2 dissociation into CO_{ads} and O_{ads} than Ni (2 0 0) surface (20.3 kcal/mol). Therefore, the Ni(1 1 1) facet of highly dispersed Ni NPs (2.6 nm) in 20Ni@MIL-101(DSM) were the main active species. The potential energy diagram for CO_2 methanation on the Ni(1 1 1) plane slab structure was presented in Fig. 13d. Initially, CO_2 molecule was adsorbed on Ni(1 1 1) surface and transformed to CO_{ads} and O_{ads}. Then, CO_{ads} reacted with H to generate CH_2OH_{ads}. The OH group of CH_2OH_{ads} was then removed and reacted with H to form CH_4.

Interestingly, the precise location of the confined metal species also affected the electron transfer from metal species to MOFs. Deng et al. [119] created "molecular compartments" inside MIL-101 materials by confining TiO_2 in their different pores, which allowed for synergy between the light-absorbing/electron-producing TiO_2 units and the catalytic metal clusters in the MOFs. Generally, there were three types of pores that existed in MIL-101: 8, 29 and 34 Å, labeled as micropore, mesopore I and mesopore II, respectively. Only mesopore I and II were accessible to titanium precursors and enabled for growing TiO_2 to form molecular compartments, denoted as compartment I and II, respectively. They compared the CO_2 photoreduction activity of 42%-TiO_2-in-MIL-101-Cr, 42%-TiO_2-in-MIL-101-Cr-NH_2, 42%-TiO_2-in-MIL-101-Cr-NO_2, 42%-TiO_2-in-MIL-101-Fe and 42%-TiO_2-in-MIL-101-Al-NH_2 (the weight percent of TiO_2 content was 42%) and found the 42%-TiO_2-in-Cr-MIL-101-NO_2 showed the highest activity, the production rate of CO and CH_4 were hardly any decrease through a 60-hour test (Fig. 14a). Significantly, a fast O_2 production rate of 7.2 mmol g^{-1} can be obtained. The charge balance between the electron conversion (for CO and CH_4 generation) and the hole consumption (for O_2 production) implied the excellent charge separation. The AQE of 42%-TiO_2-in-Cr-MIL-101-NO_2 was 11.3% at 350 nm without sacrificial reagent. When the AQE values of 42%-TiO_2-in-Cr-MIL-101-NO_2 were plotted against the corresponding wavelength, the data points fell well on the absorption spectrum of pure TiO_2 NPs (Fig. 14c), while negligible reduction products were observed from pure Cr-MIL-101-NO_2 (Fig. 14b). Therefore, the TiO_2 units were responsible for the generation of excited electrons upon light irradiation. According to transient absorption spectroscopy (TAS) (Fig. 14e and f), the lifetime of excited electrons in 42%-TiO_2-in-MIL-101-Cr-NO_2 in TiO_2 was 2.47 μs, which was

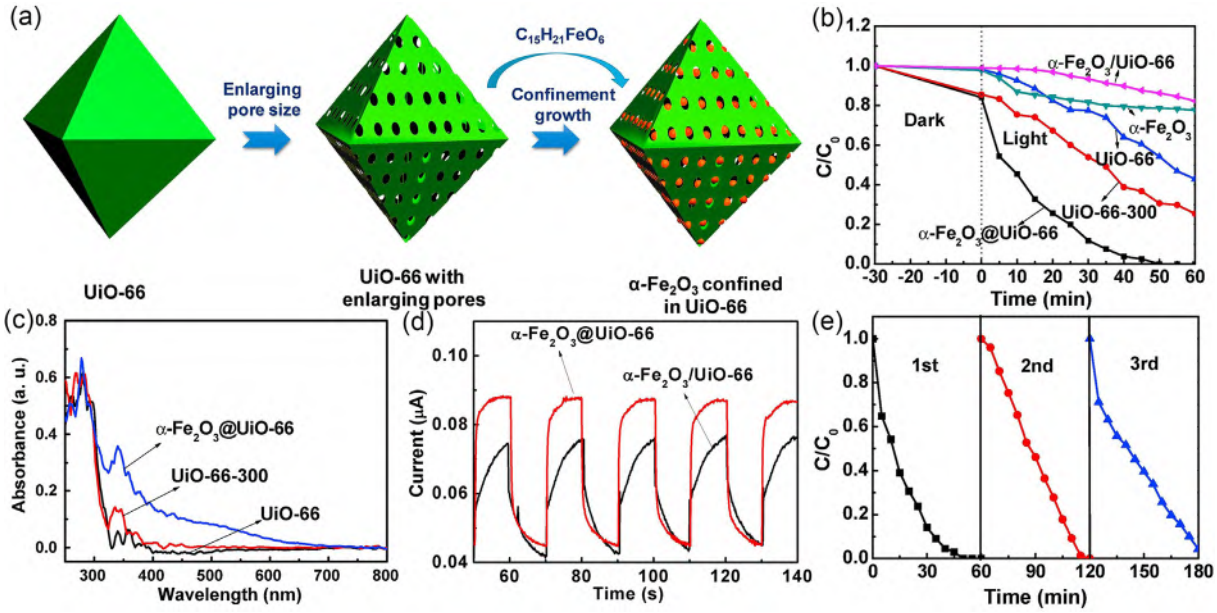

Fig. 15. (a) Scheme of preparation process of α-Fe_2O_3@UiO-66 heterostructure; (c) UV - visible light absorption spectra of the UiO-66, UiO-66-300 thermally treated at 300 °C, and α-Fe_2O_3@UiO-66 heterostructure; (d) Photocurrent curves vs. Ag/AgCl of the α-Fe_2O_3@UiO-66 heterostructure and the α- Fe_2O_3/UiO-66 prepared using $FeCl_3$ at the applied potential voltage of 0.2 V under visible-light (λ > 420 nm) irradiation; (e) time-cycle photodegradation curves of MB over α-Fe_2O_3@UiO-66 heterostructure irradiated by visible light. Reproduced with permission [31]. Copyright 2019, Elsevier.

much bigger than that of 42%-TiO_2-on-MIL-101-Cr-NO_2 (4.3×10^{-2} μs) and pure TiO_2 (P25). The location of TiO_2 units was found to be essential for the photocatalytic activity. For 42%-TiO_2-in-MIL-101-Cr-NO_2, TiO_2 units in compartment II exhibited a TOF of 5.9 h^{-1} per TiO_2 formula, 44 times more active than those in compartment I, 1.7×10^3 times of those on MIL-101-Cr-NO_2 surface (Fig. 14g). The compartmentalization strategy reduced the recombination of photo-generated charge carriers on TiO_2 surface, therefore accelerated CO_2 photoreduction.

4.3. Water remediation

The discharge of dye wastewater can reduce the aesthetic value of the water and interference with light entering the water, thus the aquatic system will be disturbed. In addition, most of dye molecules have aromatic rings that make them mutagenic and carcinogenic [120]. Generally, the dye molecules have two main groups: chromophore and auxochrome, which make them colorful [121]. However, the traditional microbial method is time-consuming and inefficient to the organic pollutants [122,123]. The photocatalytic degradation of dyes is apparent as the breaking of the chromophore and auxochrome can make the dye solution gradually colorless.

Photocatalytic degradation technology is based on the generation of active species such as singlet oxygen ($^1O_2$), superoxide radical ($O_2^{\cdot-}$), photo-generated h^+, and $HO^{\cdot}$ to transform the organic pollutants to CO_2, H_2O and other small molecular matters. The mineralization rate can be monitored by total organic carbon (TOC) analyzer. In the photocatalytic degradation process, the semiconductor is excited by light irradiation and produces photo-generated electron-hole pairs to react with H_2O, O_2 to generate the reactive species. The reactive species can react with target pollutants to generate small molecule substances, CO_2 and H_2O. The type of reactive species can be measured by trapping experiment and electron paramagnetic resonance (ESR) test [92].

The synergistic effect between MOFs and metal species can greatly increase the photocatalytic degradation efficiency. Due to the electron short mean-free path (2–4 nm), α-Fe_2O_3 showed low photocatalytic performance for the high recombination rate of photo-generated carriers. By confining α-Fe_2O_3 growth in the pores of UiO-66, the limited diameter of α-Fe_2O_3 (<2 nm) shortened the carrier transport distance and improved the photocatalytic performance towards MB irradiated with visible light that the degradation rate of the α-Fe_2O_3@UiO-66 was 23.6 times higher than that of α-Fe_2O_3 loaded on the external surface of UiO-66 [31]. The synthesis process of α-Fe_2O_3@UiO-66 was shown in Fig. 15a, of which the pristine UiO-66 was treated at 300 °C to enlarge the pores. The photocatalytic activity of samples was shown in Fig. 15b. The α-Fe_2O_3@UiO-66 showed the highest photodegradation efficiency, while almost no degradation of MB by the α-Fe_2O_3/UiO-66. The spectra of UV–visible light absorption showed the absorption band of UiO-66 was less than 300 nm while the α-Fe_2O_3@UiO-66 was around 400–600 nm (Fig. 15c). Photocurrent responses exhibited that the α-Fe_2O_3@UiO-66 had a higher photocurrent intensity than α-Fe_2O_3/UiO-66 under visible-light irradiation. The synergistic effect between UiO-66 and the confined α-Fe_2O_3 enabled a wider range of sunlight adsorption (Fig. 15c) and facilitated the transport of photogenerated electron-holes pairs (Fig. 15d). Moreover, after recycled three times, the photodegradation efficiency had hardly decay (Fig. 15e). Wu et al. [124] found that the confined Pd NPs in UiO-66(NH_2) showed enhanced photocatalytic activity towards Cr(VI) reduction and methyl orange (MO) and methylene blue (MB) degradation. The broadened light absorption intensity, extended lifetime of photogenerated charge carriers and increased surface area resulted in higher photoactivity.

5. Conclusion and outlook

In this review, the recent progress in fabrication of metal species@MOFs and the advanced characterizations to characterize the relative location between metal species and MOFs was summarized. The synthetic strategy can be divided into four parts, including prefabrication of MOFs, pro-fabrication of MOFs, one-pot fabrication and self-sacrifice method. The confinement strategy of MOFs limits the growth of metal species and stabilizes them

in the pores with high dispersion. In addition, the photocatalytic application of metal species@MOFs in energy and environment (H_2 generation, CO_2 reduction and water remediation), the synergistic effects of the two components are discussed. The confinement strategy plays an important part in obtaining metal species@MOFs photocatalyst with superior properties, such as extended light absorption, appropriate band structure, high efficiency of charge mobility, enhanced stability and increased mass-transfer efficiency.

Though great achievements have been made so far, several problems need to be solved: (i) The designing of efficient metal species@MOFs photocatalyst has developed promptly in recent years, and the combination of computation and experiment seems to be a potential way for high-throughput screening of metal species@MOFs photocatalyst. Big data mining technology can be used to guide the fabrication of high-performance metal species@MOFs photocatalyst [112]. (ii) The weak coordination bonds between metal sites and organic linkers in MOFs determines their metastable property, which limits their practical applications. There are several ideas to increase the stability of MOFs such as using highly acidic metal or highly basic ligand to form strong metal–ligand bond and functionalizing the organic ligand to shield the metal–ligand bond from interactions with exogenous molecules. (iii) The confinement of metal species that match the pore size of MOFs with a definite spatial dispersion is challenging. In addition, it is difficult to quantitatively analyze how many particles are in/out of the pores. (iv) At present, the theoretical calculation can be used to construct catalysts with different structures and compositions, explore the factors on the catalytic activity and study the possible reaction path, while there is little knowledge on the interactions between the confined metal species and MOFs from the experiment. The in-situ/operando characterizations combined with theoretical calculation should be applied to understand the synergetic effects. (v) Though the metal species@MOFs show superb activity, the synthetic process is usually complicated and the yield is low, which cannot be industrially produced. We believe a high potential for the commercial application of metal species@MOFs photocatalyst and hope this review can offer a reference for the pioneering follow-up research work.

CRediT authorship contribution statement

Jiao Cao: Conceptualization, Writing - original draft. **Zhaohui Yang:** Supervision, Resources, Writing - review & editing, Project administration. **Weiping Xiong:** Investigation, Writing - review & editing. **Yaoyu Zhou:** Visualization, Writing - review & editing. **You Wu:** Writing - review & editing. **Meiying Jia:** Writing - review & editing. **Chengyun Zhou:** Visualization, Writing - review & editing. **Zhengyong Xu:** Writing - review & editing.

Declaration of Competing Interest

The authors declare that they have no known competing financial interests or personal relationships that could have appeared to influence the work reported in this paper.

Acknowledgement

This work was supported by the National Natural Science Foundation of China [Grant numbers: 51578223, 51521006 and 51709103].

References

[1] Z.W. Seh, J. Kibsgaard, C.F. Dickens, I. Chorkendorff, J.K. Nørskov, T.F. Jaramillo, Science 355 (2017) 4998–5011.
[2] W. Zhang, A.R. Mohamed, W.J. Ong, Angew. Chem. Int. Ed. 59 (2020) 22894–22915.
[3] A. Banerjee, K.E. Halvorsen, A. Eastmond-Spencer, S.R. Sweitz, Environ. Manage. 59 (2017) 912–923.
[4] T. Zeng, M. Yu, H. Zhang, Z. He, J. Chen, S. Song, Catal. Sci. Technol. 7 (2017) 396–404.
[5] J. Liu, Y.-Z. Fan, K. Zhang, L. Zhang, C.-Y. Su, J. Am. Chem. Soc. 142 (2020) 14548–14556.
[6] U. Shanker, M. Rani, V. Jassal, Environ. Chem. Lett. 15 (2017) 623–642.
[7] D. Ringe, G.A. Petsko, Science 320 (2008) 1428–1429.
[8] Q. Fu, X. Bao, Nat. Catal. 2 (2019) 834–836.
[9] G. Zhou, B. Wang, R. Cao, J. Am. Chem. Soc. 142 (2020) 14848–14853.
[10] S. Zhou, X. Yang, X. Xu, S.X. Dou, Y. Du, J. Zhao, J. Am. Chem. Soc. 142 (2019) 308–317.
[11] L. Liu, M. Lopez-Haro, C.W. Lopes, C. Li, P. Concepcion, L. Simonelli, J.J. Calvino, A. Corma, Nat. Mater. 18 (2019) 866–873.
[12] W. Lu, R. Jiang, X. Yin, L. Wang, Nano Res. 12 (2019) 159–163.
[13] J. Cao, Z. Yang, W. Xiong, Y. Zhou, Y. Wu, M. Jia, S. Sun, C. Zhou, Y. Zhang, R. Zhong, Sep. Purif. Technol. 250 (2020) 117237–117246.
[14] J. Xiao, X. Pan, S. Guo, P. Ren, X. Bao, J. Am. Chem. Soc. 137 (2015) 477–482.
[15] Z. Yang, J. Qian, A. Yu, B. Pan, Proc. Natl. Acad. Sci. 116 (2019) 6659–6664.
[16] L. Han, X. Liu, J. Chen, R. Lin, H. Liu, F. Lü, S. Bak, Z. Liang, S. Zhao, E. Stavitski, J. Luo, R.R. Adzic, H.L. Xin, Angew. Chem. Int. Ed. 58 (2019) 2321–2325.
[17] L. Chen, Q. Xu, Matter 1 (2019) 57–89.
[18] X. Zhang, H. Liu, Y. Shi, J. Han, Z. Yang, Y. Zhang, C. Long, J. Guo, Y. Zhu, X. Qiu, G. Xue, L. Zhang, B. Zhang, L. Chang, Z. Tang, Matter 3 (2020) 558–570.
[19] Q. Yang, W. Liu, B. Wang, W. Zhang, X. Zeng, C. Zhang, Y. Qin, X. Sun, T. Wu, J. Liu, F. Huo, J. Lu, Nat. Commun. 8 (2017) 14429–14437.
[20] K. Choe, F. Zheng, H. Wang, Y. Yuan, W. Zhao, G. Xue, X. Qiu, M. Ri, X. Shi, Y. Wang, G. Li, Z. Tang, Angew. Chem. Int. Ed. 59 (2020) 3650–3657.
[21] C. Xu, R. Fang, R. Luque, L. Chen, Y. Li, Coord. Chem. Rev. 388 (2019) 268–292.
[22] A.R. Riscoe, C.J. Wrasman, A.A. Herzing, A.S. Hoffman, A. Menon, A. Boubnov, M. Vargas, S.R. Bare, M. Cargnello, Nat. Catal. 2 (2019) 852–863.
[23] L. Chen, R. Luque, Y. Li, Dalton Trans. 47 (2018) 3663–3668.
[24] L. Chen, R. Luque, Y. Li, Chem. Soc. Rev. 46 (2017) 4614–4630.
[25] P. Ji, Y. Song, T. Drake, S.S. Veroneau, Z. Lin, X. Pan, W. Lin, J. Am. Chem. Soc. 140 (2018) 433–440.
[26] M. Jia, Z. Yang, H. Xu, P. Song, W. Xiong, J. Cao, Y. Zhang, Y. Xiang, J. Hu, C. Zhou, Y. Yang, W. Wang, Chem. Eng. J. 388 (2020) 124388–124401.
[27] M. Yoon, R. Srirambalaji, K. Kim, Chem. Rev. 112 (2012) 1196–1231.
[28] A. Lin, A.A. Ibrahim, P. Arab, H.M. El-Kaderi, M.S. El-Shall, ACS Appl. Mater. Interfaces 9 (2017) 17961–17968.
[29] J.-J. Ye, C.-D. Wu, Dalton Trans. 45 (2016) 10101–10112.
[30] C.R. Kim, T. Uemura, S. Kitagawa, Chem. Soc. Rev. 45 (2016) 3828–3845.
[31] R. Zhang, B. Du, Q. Li, Z. Cao, G. Feng, X. Wang, Appl. Surf. Sci. 466 (2019) 956–963.
[32] A.M. Abdel-Mageed, B. Rungtaweevoranit, M. Parlinska-Wojtan, X. Pei, O.M. Yaghi, R.J. Behm, J. Am. Chem. Soc. 141 (2019) 5201–5210.
[33] S. Aslam, F. Subhan, Z. Yan, U. Etim, J. Zeng, Chem. Eng. J. 315 (2017) 469–480.
[34] S.E. Bozbağ, C. Erkey, J. Supercritical Fluids 96 (2015) 298–312.
[35] K. Matsuyama, M. Motomura, T. Kato, T. Okuyama, H. Muto, Microporous Mesoporous Mater. 225 (2016) 26–32.
[36] S. Xiang, L. Cai, in: 2010 IEEE Global Telecommunications Conference GLOBECOM 2010, 1-5.
[37] L. Chen, Y. Wang, F. Yu, X. Shen, C. Duan, J. Mater. Chem. A 7 (2019) 11355–11361.
[38] T.J. Wilke, M.A. Barteau, J. Catal. 382 (2020) 286–294.
[39] M. Samaniyan, M. Mirzaei, R. Khajavian, H. Eshtiagh-Hosseini, C. Streb, ACS Catal. 9 (2019) 10174–10191.
[40] G. Huang, L. Yang, Q. Yin, Z.-B. Fang, X.-J. Hu, A.-A. Zhang, J. Jiang, T.-F. Liu, R. Cao, Angew. Chem. Int. Ed. 132 (2020) 4415–4420.
[41] Q. Liu, Y. Li, Y. Fan, C.-Y. Su, G. Li, J. Mater. Chem. A 8 (2020) 11442–11447.
[42] H. Zhang, M. Huang, J. Wen, Y. Li, A. Li, L. Zhang, A.M. Ali, Y. Li, Chem. Commun. 55 (2019) 4699–4702.
[43] J. Li, Q.-L. Zhu, Q. Xu, Catal. Sci. Technol. 5 (2015) 525–530.
[44] Q.-L. Zhu, J. Li, Q. Xu, J. Am. Chem. Soc. 135 (2013) 10210–10213.
[45] J. Jin, Z. Yang, W. Xiong, Y. Zhou, R. Xu, Y. Zhang, J. Cao, X. Li, C. Zhou, Sci. Total Environ. 650 (2019) 408–418.
[46] Y.-Z. Chen, Q. Xu, S.-H. Yu, H.-L. Jiang, Small 11 (2015) 71–76.
[47] H.R. Moon, M.P. Suh, Eur. J. Inorg. Chem. 2010 (2010) 3795–3803.
[48] J. Su, S. Yuan, T. Wang, C.T. Lollar, J.-L. Zuo, J. Zhang, H.-C. Zhou, Chem. Sci. 11 (2020) 1918–1925.
[49] K. Wenderich, G. Mul, Chem. Rev. 116 (2016) 14587–14619.
[50] M.S. El-Shall, V. Abdelsayed, A.E.R.S. Khder, H.M.A. Hassan, H.M. El-Kaderi, T. E. Reich, J. Mater. Chem. 19 (2009) 7625–7631.
[51] J.E. Mondloch, W. Bury, D. Fairen-Jimenez, S. Kwon, E.J. DeMarco, M.H. Weston, A.A. Sarjeant, S.T. Nguyen, P.C. Stair, R.Q. Snurr, O.K. Farha, J.T. Hupp, J. Am. Chem. Soc. 135 (2013) 10294–10297.
[52] P.-Z. Li, K. Aranishi, Q. Xu, Chem. Commun. 48 (2012) 3173–3175.
[53] J. Hermannsdörfer, M. Friedrich, N. Miyajima, R.Q. Albuquerque, S. Kümmel, R. Kempe, Angew. Chem. Int. Ed. 51 (2012) 11473–11477.
[54] I.S. Kim, Z. Li, J. Zheng, A.E. Platero-Prats, A. Mavrandonakis, S. Pellizzeri, M. Ferrandon, A. Vjunov, L.C. Gallington, T.E. Webber, N.A. Vermeulen, R.L. Penn, R.B. Getman, C.J. Cramer, K.W. Chapman, D.M. Camaioni, J.L. Fulton, J.A. Lercher, O.K. Farha, J.T. Hupp, A.B.F. Martinson, Angew. Chem. Int. Ed. 57 (2018) 909–913.

[55] C.-W. Kung, C.O. Audu, A.W. Peters, H. Noh, O.K. Farha, J.T. Hupp, ACS Energy Lett. 2 (2017) 2394–2401.
[56] I.S. Kim, S. Ahn, N.A. Vermeulen, T.E. Webber, L.C. Gallington, K.W. Chapman, R.L. Penn, J.T. Hupp, O.K. Farha, J.M. Notestein, A.B.F. Martinson, J. Am. Chem. Soc. 142 (2020) 242–250.
[57] X. Zhao, L. Gong, C. Wang, C. Wang, K. Yu, B. Zhou, Chem. - A Eur. J. 26 (2020) 4613–4619.
[58] M. Rubio-Martinez, C. Avci-Camur, A.W. Thornton, I. Imaz, D. Maspoch, M.R. Hill, Chem. Soc. Rev. 46 (2017) 3453–3480.
[59] T. Ishida, M. Nagaoka, T. Akita, M. Haruta, Chemistry (Weinheim an der Bergstrasse Germany) 14 (2008) 8456–8460.
[60] R. Mahugo, A. Mayoral, M. Sánchez-Sánchez, I. Diaz, Front. Chem. 7 (7) (2019) 686–697.
[61] D. Rambabu, S. Bhattacharyya, T. Singh, C. M. L, T.K. Maji, Inorganic Chemistry, 59 (2020) 1436-1443.
[62] Y. Chen, S. Li, X. Pei, J. Zhou, X. Feng, S. Zhang, Y. Cheng, H. Li, R. Han, B. Wang, Angew. Chem. Int. Ed. 55 (2016) 3419–3423.
[63] G. Li, K. Zhang, C. Li, R. Gao, Y. Cheng, L. Hou, Y. Wang, Appl. Catal. B 245 (2019) 753–759.
[64] G. Li, S. Zhao, Y. Zhang, Z. Tang, Adv. Mater. 30 (2018) 1800702–1800744.
[65] C.L. Whitford, C.J. Stephenson, D.A. Gómez-Gualdrón, J.T. Hupp, O.K. Farha, R. Q. Snurr, P.C. Stair, J. Phys. Chem. C 121 (2017) 25079–25091.
[66] G. Lu, S. Li, Z. Guo, O.K. Farha, B.G. Hauser, X. Qi, Y. Wang, X. Wang, S. Han, X. Liu, J.S. DuChene, H. Zhang, Q. Zhang, X. Chen, J. Ma, S.C.J. Loo, W.D. Wei, Y. Yang, J.T. Hupp, F. Huo, Nat. Chem. 4 (2012) 310–316.
[67] Q. Yang, Q. Xu, S.-H. Yu, H.-L. Jiang, Angew. Chem. Int. Ed. 55 (2016) 3685–3689.
[68] S. Wang, Y. Yu, J. Yu, T. Wang, P. Wang, Y. Li, X. Zhang, L. Zhang, Z. Hu, J. Chen, Y. Fu, W. Qi, Nanotechnology 31 (2020) 255604.
[69] X. Li, Z. Zhang, W. Xiao, S. Deng, C. Chen, N. Zhang, J. Mater. Chem. A 7 (2019) 14504–14509.
[70] B. Han, X. Hu, M. Yu, T. Peng, Y. Li, G. He, RSC Adv. 8 (2018) 22748–22754.
[71] H. Liu, L. Chang, L. Chen, Y. Li, J. Mater. Chem. A 3 (2015) 8028–8033.
[72] H. Liu, L. Chang, C. Bai, L. Chen, R. Luque, Y. Li, Angew. Chem. Int. Ed. 55 (2016) 5019–5023.
[73] W. Xiang, Y. Zhang, H. Lin, C.J. Liu, Molecules (Basel, Switzerland), 22 (2017) 2103-2126.
[74] L. Chen, H. Chen, R. Luque, Y. Li, Chem. Sci. 5 (2014) 3708–3714.
[75] L. Chen, X. Chen, H. Liu, Y. Li, Small 11 (2015) 2642–2648.
[76] L. Chen, X. Chen, H. Liu, C. Bai, Y. Li, J. Mater. Chem. A 3 (2015) 15259–15264.
[77] M. Mukoyoshi, H. Kobayashi, K. Kusada, M. Hayashi, T. Yamada, M. Maesato, J. M. Taylor, Y. Kubota, K. Kato, M. Takata, T. Yamamoto, S. Matsumura, H. Kitagawa, Chem. Commun. 51 (2015) 12463–12466.
[78] R. Cao, J.-D. Yi, R. Xie, Z.-L. Xie, G.-L. Chai, T.-F. Liu, R.-P. Chen, Y.-B. Huang, Angew. Chem. Int. Ed. 10 (2020) 601–608.
[79] Y.-Z. Chen, B. Gu, T. Uchida, J. Liu, X. Liu, B.-J. Ye, Q. Xu, H.-L. Jiang, Nat. Commun. 10 (2019) 3462–3471.
[80] Q.-C. Shang, X.-Z. Fang, H.-L. Jiang, Q. Zhang, Chin. J. Chem. Phys. 31 (2018) 613–618.
[81] M.R. Jorgensen, V.R. Hathwar, N. Bindzus, N. Wahlberg, Y.S. Chen, J. Overgaard, B.B. Iversen, IUCr J. 1 (2014) 267–280.
[82] H. Kasai, K. Tolborg, M. Sist, J. Zhang, V.R. Hathwar, M.Ø. Filsø, S. Cenedese, K. Sugimoto, J. Overgaard, E. Nishibori, B.B. Iversen, Nat. Mater. 17 (2018) 249–252.
[83] J. Cure, E. Mattson, K. Cocq, H. Assi, S. Jensen, K. Tan, M. Catalano, S. Yuan, H. Wang, L. Feng, P. Zhang, S. Kwon, J.-F. Veyan, Y. Cabrera, G. Zhang, J. Li, M. Kim, H.-C. Zhou, Y.J. Chabal, T. Thonhauser, J. Mater. Chem. A 7 (2019) 17536–17546.
[84] C.V. Cushman, P. Brüner, J. Zakel, G.H. Major, B.M. Lunt, N.J. Smith, T. Grehl, M. R. Linford, Anal. Methods 8 (2016) 3419–3439.
[85] H.-L. Jiang, Q.-P. Lin, T. Akita, B. Liu, H. Ohashi, H. Oji, T. Honma, T. Takei, M. Haruta, Q. Xu, Chem. – Eur. J. 17 (2011) 78–81.
[86] E. Brunner, M. Rauche, Chem. Sci. 11 (2020) 4297–4304.
[87] T.W. Kemnitzer, C.B. Tschense, T. Wittmann, E.A. Rössler, J.r. Senker, Langmuir, 34 (2018) 12538-12548.
[88] L.H. Cong, B.C. Gu, X.X. Han, Q.H. Zhao, Z.W. Pan, R. Ye, J.Q. Guo, B.J. Ye, Nuclear Instruments and Methods in Physics Research Section A: Accelerators, Spectrometers, Detectors and Associated Equipment 946 (2019) 162691–162696.
[89] D. Li, M. Kassymova, X. Cai, S.-Q. Zang, H.-L. Jiang, Coord. Chem. Rev. 412 (2020) 213262–213277.
[90] M. Xiao, Z. Wang, M. Lyu, B. Luo, S. Wang, G. Liu, H.-M. Cheng, L. Wang, Adv. Mater. 31 (2019) 1801369–1801391.
[91] J. Cao, Z.-H. Yang, W.-P. Xiong, Y.-Y. Zhou, Y.-R. Peng, X. Li, C.-Y. Zhou, R. Xu, Y.-R. Zhang, Chem. Eng. J. 353 (2018) 126–137.
[92] C. Dai, B. Liu, Energy Environ. Sci. 13 (2020) 24–52.
[93] Y. Liu, Y. Cheng, H. Zhang, M. Zhou, Y. Yu, S. Lin, B. Jiang, X. Zhao, L. Miao, C.-W. Wei, Q. Liu, Y.-W. Lin, Y. Du, C.J. Butch, H. Wei, Sci. Adv. 6 (2020) 2695–2705.
[94] Y. Liu, S. Liu, S. Liu, D. Liang, S. Li, Q. Tang, X. Wang, J. Miao, Z. Shi, Z. Zheng, Chem. Cat. Chem. 5 (2013) 3086–3091.
[95] Y. Luo, Q. Wang, J. Li, F. Xu, L. Sun, Y. Zou, H. Chu, B. Li, K. Zhang, Mater. Today Nano 9 (2020) 100071–100116.
[96] D. Wang, Z. Li, J. Catal. 342 (2016) 151–157.
[97] A. Zada, P. Muhammad, W. Ahmad, Z. Hussain, S. Ali, M. Khan, Q. Khan, M. Maqbool, Adv. Funct. Mater. 30 (2020) 1906744–1906772.
[98] Y. Gao, F. Cheng, W. Fang, X. Liu, S. Wang, W. Nie, R. Chen, S. Ye, J. Zhu, H. An, C. Fan, F. Fan, C. Li, Natl. Sci. Rev. 10 (2020) 151–175.
[99] C.-C. Hou, H.-F. Wang, C. Li, Q. Xu, Energy Environ. Sci. 13 (2020) 1658–1693.
[100] M. Karayilan, W.P. Brezinski, K.E. Clary, D.L. Lichtenberger, R.S. Glass, J. Pyun, Angew. Chem. Int. Ed. 58 (2019) 7537–7550.
[101] H.-L. Jiang, K. Sun, M. Liu, J. Pei, D. Li, C. Ding, K. Wu, Angew. Chem. Int. Ed. 59 (2020) 22749–22755.
[102] X. Fang, Q. Shang, Y. Wang, L. Jiao, T. Yao, Y. Li, Q. Zhang, Y. Luo, H.-L. Jiang, Adv. Mater. 30 (2018) 1705112–1705118.
[103] X. Chen, S. Shen, L. Guo, S.S. Mao, Chem. Rev. 110 (2010) 6503–6570.
[104] J.-D. Xiao, Q. Shang, Y. Xiong, Q. Zhang, Y. Luo, S.-H. Yu, H.-L. Jiang, Angew. Chem. Int. Ed. 55 (2016) 9389–9393.
[105] S. Li, H.-M. Mei, S.-L. Yao, Z.-Y. Chen, Y.-L. Lu, L. Zhang, C.-Y. Su, Chem. Sci. 10 (2019) 10577–10585.
[106] P. Karthik, E. Balaraman, B. Neppolian, Catal. Sci. Technol. 8 (2018) 3286–3294.
[107] K. Sun, M. Liu, J. Pei, D. Li, C. Ding, K. Wu, H.-L. Jiang, Angew. Chem. Int. Ed. 59 (2020) 22749–22755.
[108] C. Liu, G. Zhang, L. Yu, J. Qu, H. Liu, Small 14 (2018) 1800421–1800429.
[109] Y. Han, H. Xu, Y. Su, Z.-L. Xu, K. Wang, W. Wang, J. Catal. 370 (2019) 70–78.
[110] Z. Sun, N. Talreja, H. Tao, J. Texter, M. Muhler, J. Strunk, J. Chen, Angew. Chem. Int. Ed. 57 (2018) 7610–7627.
[111] X. Li, Q.-L. Zhu, Energy Chem. 2 (2020) 100033–100061.
[112] P.G. Boyd, A. Chidambaram, E. García-Díez, C.P. Ireland, T.D. Daff, R. Bounds, A. Gładysiak, P. Schouwink, S.M. Moosavi, M.M. Maroto-Valer, J.A. Reimer, J.A. R. Navarro, T.K. Woo, S. Garcia, K.C. Stylianou, B. Smit, Nature 576 (2019) 253–256.
[113] Y. Wang, N.-Y. Huang, J.-Q. Shen, P.-Q. Liao, X.-M. Chen, J.-P. Zhang, J. Am. Chem. Soc. 140 (2018) 38–41.
[114] L.-Y. Wu, Y.-F. Mu, X.-X. Guo, W. Zhang, Z.-M. Zhang, M. Zhang, T.-B. Lu, Angew. Chem. Int. Ed. 58 (2019) 9491–9495.
[115] M. Chen, L. Han, J. Zhou, C. Sun, C. Hu, X. Wang, Z. Su, Nanotechnology 29 (2018) 284003–2840012.
[116] W. Zhen, B. Li, G. Lu, J. Ma, Chem. Commun. 51 (2015) 1728–1731.
[117] Z.-H. Yan, B. Ma, S.-R. Li, J. Liu, R. Chen, M.-H. Du, S. Jin, G.-L. Zhuang, L.-S. Long, X.-J. Kong, L.-S. Zheng, Sci. Bullet. 64 (2019) 976–985.
[118] W. Zhen, F. Gao, B. Tian, P. Ding, Y. Deng, Z. Li, H. Gao, G. Lu, J. Catal. 348 (2017) 200–211.
[119] Z. Jiang, X. Xu, Y. Ma, H.S. Cho, D. Ding, C. Wang, J. Wu, P. Oleynikov, M. Jia, J. Cheng, Y. Zhou, O. Terasaki, T. Peng, L. Zan, H. Deng, Nature 586 (2020) 549–554.
[120] A. Mittal, J. Mittal, A. Malviya, D. Kaur, V.K. Gupta, J. Colloid Interface Sci. 343 (2010) 463–473.
[121] A. Nasar, F. Mashkoor, Environ. Sci. Pollut. Res. 26 (2019) 5333–5356.
[122] N. Le-Minh, S.J. Khan, J.E. Drewes, R.M. Stuetz, Water Res. 44 (2010) 4295–4323.
[123] J. Cao, S. Sun, X. Li, Z. Yang, W. Xiong, Y. Wu, M. Jia, Y. Zhou, C. Zhou, Y. Zhang, Chem. Eng. J. 382 (2020) 122802–122813.
[124] L. Shen, W. Wu, R. Liang, R. Lin, L. Wu, Nanoscale 5 (2013) 9374–9382.